Investigating neutrino production in Swift J1644+57

O Rabyang

orcid.org 0000-0002-6231-1918

Dissertation accepted in partial fulfilment of the requirements for the degree *Master of Science in Astrophysical Sciences* at the North-West University

Supervisor: Prof M Böttcher

Graduation December 2020

27743268

"When you carry out an experiment there are two possible outcomes either you confirm the threshold expectation, and in this case you made a measurement, or you don't, and in this case you made a discovery."

Enrico Fermi

"Neutrino physics is largely an art of learning a great deal by observing nothing."

Haim Harari

NORTH-WEST UNIVERSITY, POTCHEFSTROOM CAMPUS

Abstract

Faculty Name
Centre for Space Research

Masters Dissertation

Neutrino productions in tidal disruption events.

by Omphile RABYANG

The recent detection of astrophysical very-high-energy neutrinos by IceCube has spurred an intensive search for their sources. As possible sources of VHE neutrinos, tidal disruption events (TDEs) have been suggested. Here we investigate a jetted TDE - Swift J1644+57 which is the best measured TDE in multiple wavebands - as a candidate astrophysical neutrino source. TDEs occur when a star approaches a massive black hole located at the centre of a galaxy. If the tidal radius is larger than the Swarzschild radius of the super massive black hole (SMBH) this leads to tidal forces violently disrupting the star. Matter accretes on the SMBH and produces luminous and long-lasting flares. We investigate the neutrino production in the TDE emission region using a hadronic code. This is done through a parameter study based on fits to the spectral energy distribution (SED) of the source, evaluating the expected neutrino detection rate by IceCube. We explore how the expected neutrino detection rate depends on various parameters. The radiation transfer code produced the required fits for $B = 60, 70, 80, 90$ and 100 G with blob radius varying from $R_{blob} = 10^{15}, 10^{16}$ to 10^{17} cm. All the model fits in this study require bulk kinetic jet powers in the relativistic protons in the range $L_p \sim 10^{47} - 10^{52} erg.s^{-1}$. In the parameter study we noticed that when we set constant $R_{blob} = 10^{15} cm$ the neutrino detection probability is $t_\nu = 1 \times 10^{-7}$ and $t_\nu = 2 \times 10^{-8}$ for $B = 60G$ and $B = 100G$, respectively. The parameter study shows that there is an anti-correlation between the magnetic field and the neutrino detection probability. Our study suggests that X-ray bright jetted TDEs are weak neutrino producing sites.

Acknowledgements

The Bushmen in the Kalahari Desert spoke of the two "hungers". There is the Great Hunger and there is the Little Hunger. The Little Hunger wants food for the belly; but the Great Hunger, the greatest hunger of all, is the hunger for meaning. Below is a token of appreciation to all the people who continue to help me fulfil my Great Hunger.

I wish to express my sincere appreciation to my supervisor, Professor Markus B*ö*ttcher, thank you for investing your time and departing your knowledge with me. It has truly been an honour to work with a world class scientist of your distinction. Foteini Oikonomou it is with whole-hearted appreciation for the great advice which proved to be monumental towards the success of this project. Jabus van den Berg, Michael Kreter and Timothy Mohlolo I would like to recognize the invaluable assistance that you all provided during my study. Lent*è* Dreyer, thank you for helping me keep sane throughout this process. I wish to also show my gratitude to Petro Sieberhagen and my colleagues at the Centre for Space Research for always making the department feel like a home away from home. To the High Energy Astrophysics group your passion and curiosity has been a constant lighthouse throughout my journey. To my friends and family there isn't enough gratitude which I could use to express my appreciation for your presence in my life. I am because you are. Your conversations and jokes keeps my life entertained and colourful. All of this would have not been possible without the funding from the National Astrophysics and Space Science Programme (NASSP), National Research Foundation (NRF) and the Department of Science and Innovation (DSI). To my mother, Kea leboga! I am thankful for the woman that you are. The teacher, sister, citizen and lastly mother that you are. You are an exemplary human being. Thank you for allowing me to be myself, for the affirmations and thank you for the tough love when necessary. In conclusion I would like to dedicate this dissertation to my grandmother Botshe Christina Kabelo (ne*è* Molete). Mama, I know where ever you are; you are proud. Thank you for the teachings and sacrifices which you made. This is not my win but ours because I stand on the shoulders of great giants.

Kwena ! A e boele metsing.

Pula!

Contents

Acknowledgements **v**

1 Introduction **1**

2 Theoretical background **5**
2.1 Neutrinos and Neutrino astronomy 5
2.1.1 Neutrino kinematics 7
2.2 Relativistic kinematics and cross sections 9
2.3 Neutrino detection 12
2.4 Tidal disruption events 15
2.4.1 The Newtonian picture 17
2.4.2 Observations of Swift J1644+57 21
2.4.3 Magnetic fields in TDEs 22
2.4.4 The role of the accretion flow 23
2.4.5 Particle acceleration within the jets 27

3 Model set-up **31**
3.1 Radiation processes 33
3.1.1 Electron Synchrotron 33
3.1.2 Proton Synchrotron 34
3.1.3 Electromagnetic cascades in jets. 35
3.2 Expected neutrino detection probability 36

4 Results and Evaluation of results **39**

5 Conclusion **49**

Bibliography **51**

List of Figures

1.1 The role of neutrinos as messengers in high energy astrophysics. Energetic astrophysical environments may be the sources for the emission of high energy cosmic ray particles, gamma rays and high energy neutrinos. The particles (p, e) are deflected by intergalactic magnetic fields and lose their directional information by the time they are detected. Gamma rays ($\gamma-$rays) are attenuated by interstellar dust clouds and interactions with the cosmic background radiation. The neutrinos (ν) travel through the Universe freely and point back to their source of origin when they are detected on Earth. Courtesy: Dumm 2011 3

2.1 Lower-energy photons can travel to Earth from the extragalactic distances whereas high energy photons and cosmic rays are attenuated after shorter distances. Therefore, obscuring our view of the most energetic astrophysical events. In contrast, gravitational waves (GW) and neutrinos can travel through the Universe without being attenuated or deflected. Hence, GW and neutrinos make suitable probes of the high-energy sky. Credit: Shawhan 2018 6

2.2 The relationship between neutrino energies and their cross-section depending on the cosmological source from which they originate. The higher the neutrino energies, the more likely its interaction with regular matter, hence a relatively larger cross-section. The peak at 10^{16} eV is due to the Glashow resonance, which occurs when ultra-high energy electron anti-neutrinos allow the resonant formation of W^- in their interactions with electrons at 6.3 PeV. Credit: Formaggio and Zeller 2012 7

2.3 The Feynman diagrams showing the high-energy neutrino interactions of neutral current (NC) and charged current (CC). Credit: Abreu et al. 2011 13

2.4 These are the different event signatures in the detector. Neutral current and charged current interactions involving ν_e produce a cascade-like signature. Events forming due to charged current interactions of ν_μ are represented by track-like signatures, whereas the ν_τ charge current interactions have a "double bang" signature. Credit : Madsen 2019 14

2.5 (I)When a star with mass, M_*, and radius, R_*, approaches a SMBH of mass, M_{BH}. (II) In the event of a star being disrupted, approximately half of the stellar debris will be bound to the SMBH (orange). (III) The more bound matter could accrete onto the black hole (BH), although there is a prospect that shocks from returning material could unbind some of the matter. Credit: Müller (2007) 16

2.6 The parameter space of a tidal disruption within the Newtonian regime. These three triangles represent solar-type stars (blue, dashed) red giants with $M_* = M_\odot$, $R_* = 10R_\odot$ (red, solid), and white dwarfs with $M_* = M_\odot$, $R_* = 10^{-2}R_\odot$ (black, dotted). Only stars in their respective triangles may undergo a tidal disruption. When $\beta < 1$ the tidal encounters are only partial disruptions implying that mass is partially stripped from the star, this occurs in the area below the triangle . If the stars encounter a BH which is larger than its Hills mass limit (equation (2.19)) then the star will be swallowed whole.This will happen if and only if the star is within the upper right corner. The upper left corner describes engulfment of small BH by a star. White dwarfs, solar-type stars and red giants may reach maximum β values 13, 62 and 133, respectively. 19
2.7 A light curve of two jetted TDEs Swift J1644+57 (blue, green and cyan) and Swift J2058 (red). The dashed line shows the X-ray emission dropped roughly as $t^{\frac{-5}{3}}$ for both TDEs. Swift J1644+57 shows many dips at different timescales accompanied by a relatively flat trend for ten days followed by intense flares with a variability timescale of $\sim$ 100 s. After approximately 500 days there is a sudden drop in the X-ray emission likely due to the relativistic jet being switched off (Zauderer et al. 2013). 21
2.8 Scattering of a particle by a magnetized moving gas cloud. Credit:Gaisser, Engel, and Resconi 2016 27

3.1 Synchrotron emission due to a deflected particle in a magnetic field. credit : Grupen et al. 2005 33
3.2 The effective area as a function of energy in IceCube IC86 configuration. Swift J1644+57 has declination +57 34 59.7 motivating the choice of the declination. This effective area is given by the data set IC86-2011 (solid blue line) while the orange line is a fit of the blue line using MINUIT. F. Oikonomou priv. communication (also see Oikonomou et al. 2019 Section 3.4). 37

4.1 This SED was produced using the baseline parameters from Table (4.1). The total radiative output is constrained by optical and X- ray data points and by the VERITAS (red) and Fermi (blue) limits in the $\gamma-$ray regime. The black, red, brown, cyan, yellow and violet curves represent the primary electron synchrotron, SSC without $\gamma\gamma$ absorption, the total hadronic model and proton synchrotron emissions of the jet. 40
4.2 Acceleration and cooling timescales for the Swift J1644+57 SED described in Chapter (3). The red line represents the characteristic timescale of the emission region, the orange line represents the acceleration timescales whereas the cyan line represents the cooling timescales. The corresponding maximum value of the proton energy is $\sim 10^{19}$ eV. 42
4.3 The all-flavour neutrino spectrum corresponding to the baseline parameters (Table 4.1, Figure (4.1)). This neutrino spectrum peaks at $\sim 10TeV$ and has a corresponding neutrino detection rate, $t_\nu = 1 \times 10^{-7}$. 43

4.4 The SED multi-plot shows the result of varying 60 Gauss to 10^2 Gauss. The blob radius is kept constant at $R = 10^{15}$ cm while other parameters, such as the injection electron luminosity and the kinetic proton kinetic luminosity, were adjusted accordingly. 44
4.5 The superimposed all-flavour neutrino ($\nu + \bar{\nu}$) spectra with parameters corresponding to Figure (4.4) 45
4.6 SED fits with $R_{blob} = 10^{15}$ to 10^{16} and 10^{17} cm with $B = 60G$. 46
4.7 Neutrino spectra from varying blob radii corresponding to Figure (4.6) 47
4.8 The log $\epsilon_{B,p}$-log B space: The relationship between the magnetization factor and the magnetic field. As the magnetic field increases $\epsilon_{B,p}$ increases. As you move along (from left to right) the diagonal lines (constant blob radius) one is less likely to produce fits which show significant cascading components.The magnetization factors in the parameter study is $L_p > L_B$this implies that the dissipation might be due to internal shocks (Sikora et al. 2005). This shocks are responsible for particle acceleration. 47
4.9 The comparison plot shows the log-log anti-correlation between the magnetic field and neutrino detection rates. An increase in blob radius results in a vertical shift of the line representing the decline in the neutrino detection rate. 48

Chapter 1

Introduction

Astronomy has relied extensively on photon-based observations for centuries. Photons take part in electromagnetic interactions and suffer absorption and scattering within the emitting source and in the media along the line of sight. Unlike photons, neutrinos are unabsorbed and unscattered over a large distance. This is because of their weak interaction with matter, their reaction cross-section is of the order 10^{-43} cm^2, depending on the neutrino energy. Neutrinos are elusive subatomic particles, which carry no electrical charge. They propagate through dense matter and can probe the physics of cosmological objects at a distance as far as the edge of the observable Universe. Astrophysical very high-energy (VHE) (1 TeV - 10 PeV) neutrinos coupled with photons are complementary messengers, which can probe violent astrophysical processes and structural evolution of the Universe (see Figure (1.1)).

The detection of astrophysical VHE neutrinos has spurred an intensive search for their production sites. A diffuse flux of high-energy astrophysical neutrinos was discovered in 2013 by the IceCube Neutrino Observatory, which is a cubic-kilometre array buried 1.5 km beneath glacier ice located at the geographic South Pole. This revelation motivated an ongoing search to find source candidates corresponding to this diffuse neutrino flux. The arrival directions and flavour composition of these neutrinos display an isotropic diffuse flux suggesting extragalactic origins (Aartsen et al. 2015). In 2018, the IceCube Observatory reported the sighting of high-energy neutrinos with more than 5σ significance (Collaboration et al. 2018). These VHE neutrinos range from a few TeV up to 10 PeV and may originate in or near the most extreme objects in the Universe.

Wolfgang Pauli first posited neutrinos in 1930 as an answer to a scientific enigma. A very puzzling problem arose during the early days of nuclear physics when radioactive beta-decays of natural elements seemed to violate the principle of the conservation of energy. Pauli postulated that the missing energy could result from a neutral particle that was escaping detection. Introducing this theory explained many experimentally observed results accurately. Enrico Fermi coined the term neutrino in 1934, meaning "little neutral one".

There are four fundamental forces and neutrinos only interact with two of these: gravity and the weak force. The latter is responsible for the radioactive decay of atomic nuclei. Due to the small cross-sections associated with the weak force, neutrinos can travel through space barely interacting, giving neutrinos the ability to move through space barely interacting with the ambient medium. This property - which makes them good astronomical messengers - also proves to be the reason why detecting neutrinos on Earth is such a mammoth task. Approximately 100 billion neutrinos pass through every square centimetre of one's body at a given moment.

Above TeV energies and up to about 10^{17} eV neutrinos are detected predominantly through the Cherenkov effect. The Cherenkov effect occurs when charged particles passing through an optically transparent medium (water or ice) at speeds greater than the speed of light in that medium. Cosmic ray muon neutrinos, for instance, interact through neutrino-nucleon interactions in ice or water, subsequently producing charged muons. The muons will suffer an energy lose due to electromagnetic interactions with the medium leading to Cherenkov radiation. To detect astrophysical such neutrinos large volumes of natural matter, i.e. ice and water, have been transformed into Cherenkov detectors. The muons will suffer an energy loss due to electromagnetic interactions with the medium leading to Cherenkov radiation. Cherenkov photons are emitted due to local polarization along the path of travel of the charged particle with the emission of electromagnetic radiation when the polarized molecules return to their original states. The Earth is used to isolate the detector from cosmic rays and other background radiation. If the neutrino energy is above 10^{17} eV the most efficient neutrino detection methods include air scintillation techniques and large air shower arrays, where electron neutrinos have the advantage to generate showers which are distinguishable from the cosmic ray background. The background atmospheric neutrino flux, as well as the atmospheric muons, limits the sensitivity of neutrino telescopes. These exceed the measured astrophysical neutrino flux by orders of magnitude for energies below O(100TeV). The origin of the vast majority of the diffuse neutrino flux remains a mystery.

Active Galactic Nuclei (AGN) and other relativistic jet sources, such as Gamma-Ray Bursts (GRBs) and Tidal disruption events (TDEs), as well as stellar objects such as pulsars, magnetars and supernovae have been identified as potential sources of high-energy neutrinos (Bednarek, Burgio, and Montaruli 2005, Waxman 2007, Becker 2008). Extragalactic sources with relativistic jets have a low jet density. Therefore the most efficient interaction is expected to be the pγ interaction (Mannheim 1993, Waxman and Bahcall 1997,Tamborra and Ando 2015). The arrival directions and flavour composition of the IceCube neutrinos display an isotropic diffuse flux of astrophysical neutrinos of extragalactic origin (Aartsen et al. 2015). Aside from a diffuse background, before 2018, the only known extraterrestrial neutrino sources were the Sun (Davis Jr, Harmer, and Hoffman 1968) and supernova SN1987A (Burrows and Lattimer 1987). In 2017 September, the detection of the IceCube-170922A neutrino coinciding with the flaring blazar TXS 0506+056 was the first $\sim 3\sigma$ high-energy neutrino source association. This blazar, located in the constellation of Orion, is powered by a supermassive black hole (SMBH), approximately 4 billion light-years away. MAGIC (Major Atmospheric Gamma Imaging Cherenkov Telescopes) observed a steep spectrum which is in agreement with internal $\gamma\gamma$ absorption above 100 GeV. This event produced a neutrino with energy 290 TeV, thus authenticating it as a genuine connection between the multi-messenger signals.

TDEs as a possible source of extragalactic neutrinos have been discussed in the literature (e.g., Wang et al. 2011, Wang and Liu 2016, Dai, McKinney, and Miller 2015,Senno, Murase, and Mészáros 2017, Lunardini and Winter 2017, Guépin et al. 2018, Biehl et al. 2017). A recent discovery is a neutrino event, IC191001A, with neutrino energy 0.2 PeV. This event was detected on two consecutive nights, 1^{st} and 2^{nd} October 2019 by IceCube and on both nights AT2019dsg was visible. AT2019dsg is one of the brightest TDEs observed in X-rays The event had a 59% probability of having an astrophysical origin.The location from which the neutrino originated was observed, 7 hours later, by the Zwicky Transient Facility (ZWF). AT2019dsg

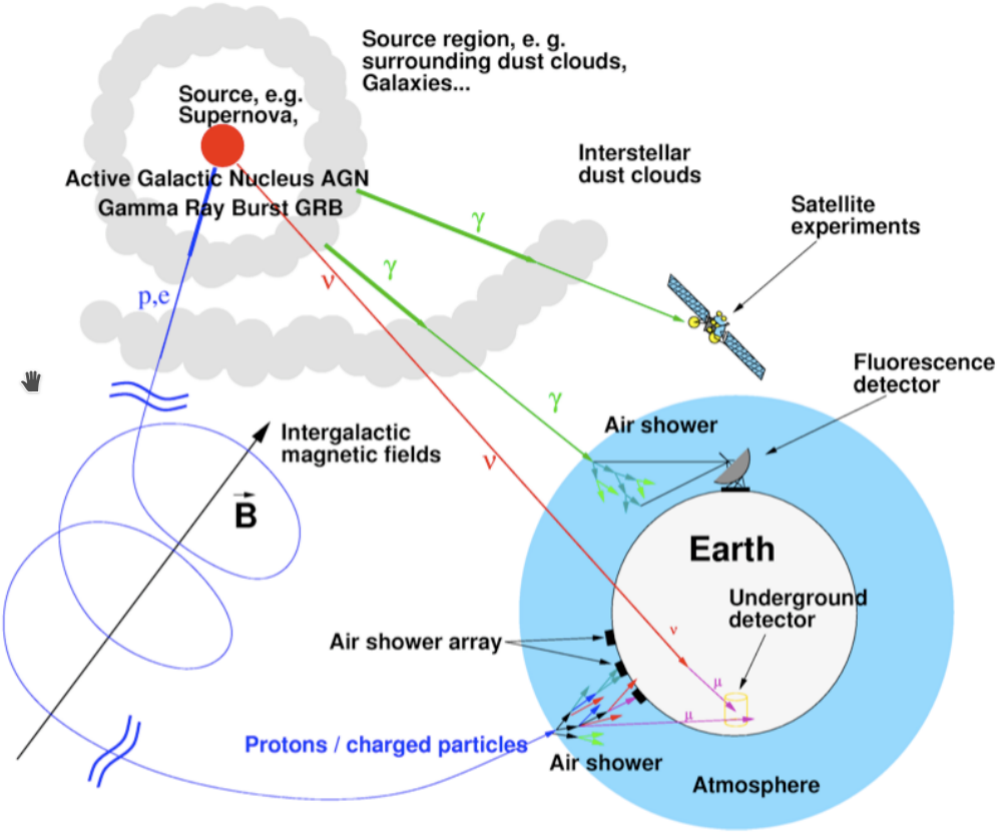

FIGURE 1.1: The role of neutrinos as messengers in high energy astrophysics. Energetic astrophysical environments may be the sources for the emission of high energy cosmic ray particles, gamma rays and high energy neutrinos. The particles (p, e) are deflected by intergalactic magnetic fields and lose their directional information by the time they are detected. Gamma rays $(\gamma-$rays) are attenuated by interstellar dust clouds and interactions with the cosmic background radiation. The neutrinos (ν) travel through the Universe freely and point back to their source of origin when they are detected on Earth. Courtesy: Dumm 2011

has been identified as a candidate neutrino source (Stein et al. 2020). An extended synchrotron-emitting outflow was detected, due to the central engine being lodged in a UV photosphere (Stein et al. 2020). In this dissertation, we explore jetted tidal disruption events (TDEs) as possible VHE neutrino producing sources. TDEs occur when the pericentre distance of a wandering star is equal to the tidal radius of a supermassive black hole (SMBH). The tidal forces of the SMBH over-power the self-binding forces of the star once the star reaches the tidal disruption radius. Approximately half of the star's debris remains bound to the black hole (BH) and finally gets accreted onto the SMBH, leading to super-Eddington accretion. TDEs with the highest mass accretion rate are likely to produce a relativistic jet [1] (Hills 1975; Rees 1988; Lacy, Townes, and Hollenbach 1982 and Phinney 1989) and exhibit a very high luminosity in the X-rays ranging from $10^{45} - 4 \times 10^{48}$ erg $\cdot$ s^{-1}. These flares can be associated with the acceleration of leptons and hadrons. If a jet is not launched, the system is referred to as a choked TDE. These powerful jets are strong enough to

1. We will refer to them as jetted TDEs or X-ray bright TDEs

accelerate protons to $10^{19} - 10^{20}$ eV (Farrar and Piran 2014). A possible acceleration site is at the shocks formed inside the jet (Blandford, Rees, and Wolfe 1978, Hardee 1979). In order for particle acceleration to occur, the timescale required for the particle acceleration must be shorter than the associated particle cooling timescale. In the literature (van Velzen et al. 2019) it has been shown that this is satisfied for a broad range of the TDE parameters. The high- energy protons accelerated by the jet interact with the soft X-ray target photon field inside the jet and subsequently produce charged pions which decay into neutrinos and other secondary particles (see Chapter 2.2). Neutrinos originating from a parent proton with energy E_P are likely to have a characteristic energy $E_\nu \sim \frac{E_P}{20}$.

In order for a source to be considered as a neutrino producing site, it must have a dense photon target field which could lead to neutrino production via photohadronic interactions. These target photons must be in the keV-MeV energy range. A measurement of O($\sim 1 - 10$) TeV neutrinos without an accompanying $\gamma-$ray emission would prove that neutrino production is occurring in the X-ray, rather than in the UV band range.

An important question that has emerged is "Are neutrinos from jetted TDEs sufficient to explain the IceCube observed flux?". Photohadronic interactions in high energy astrophysical accelerators are a crucial ingredient of hadronic models. The signature smoking gun of these interactions may be the neutrino production from charged pions, which could be detected by neutrino telescopes. In this work, we perform a parameter study of the magnetic field and blob radius of a knot moving along the jet axis of Swift J1644+57, the best-observed TDE. From this, we will study the optimal conditions under which neutrinos could be produced in TDEs. Scanning the parameter space instead of proposing a single solution leads to an estimated range of possible neutrino spectra for Swift J166+57 within the hadronic framework. We modelled the radiative output of the Swift J1644+57 jet emission numerically using the code of (Böttcher et al. 2013). Photohadronic interactions of the accelerated hadrons during the TDE X-ray flare are considered.

This thesis is organised as follows: Chapter 2 discusses the theoretical background, which serves as a basic framework of this thesis. Chapter 3 describes the model, and in Chapter 4, we present the results and discussion followed by Chapter 5, where we conclude with the implications of our results.

Chapter 2

Theoretical background

In this Chapter we will be briefly discuss the role of neutrinos as tools in multi-messenger astronomy. Additionally an explanation of how high energy neutrinos are produced and detected will also be given. For centuries astronomers have relied on electromagnetic radiation as a medium to study the Universe. Stars and galaxies are observable in the optical band whereas the Universe is transparent in the radio wavelengths all the way to X-rays and $\gamma-$rays. The $\gamma-$ rays provide a glance into the violent high energy Universe. Radiation left over from the Big Bang - the Cosmic Microwave Background (CMB)- and other radiation fields make the Universe opaque to these $\gamma-$rays due to $\gamma\gamma$ absorption,

$$\gamma + \gamma \rightarrow e^+ + e^- \tag{2.1}$$

Photons with energies $\sim$ 100 TeV significantly undergo $\gamma\gamma$ absorption. Figure (2.1) shows the distance at which the Universe becomes optically thick to photons. This occurs at energies exceeding $\sim 6 \times 10^{14}$ eV with the attenuation length being $\lambda \sim 10$ Mpc. Furthermore, cosmic rays could be used to probe the Universe. However, these energetic particles are deflected by the galactic magnetic field making it difficult to pinpoint their origins. Directional information is only conserved for very energetic protons with energies $> 10^{19}$ eV .

The observation made by the Laser Interferometer Gravitational-wave Observatory (LIGO), of gravitational waves due two merging neutron stars (Soares-Santos et al. 2017) as well as the first high energy neutrino detection by IceCube (Collaboration et al. 2013) have been pivotal in opening new windows onto the Universe. These cosmic messengers are individually produced by distinct processes, and thus carry information about different mechanisms within their source(s) of origin. Gravitational waves and neutrinos are able to pass through matter and the intergalactic magnetic fields, producing an unobstructed view of the Universe at all wavelengths.

2.1 Neutrinos and Neutrino astronomy

Neutrinos are one of the elementary particles that make up the Universe. Of the four fundamental forces in the Universe, neutrinos only interact with two of those forces - the gravitational and weak force responsible for the radioactive decay of atomic nuclei. This is because the neutrino interaction cross-sections are much smaller than those of other particles. For example, the cross-section of neutrinos ($\bar{\nu} + p \rightarrow e^+ + n$) with energies of a few MeV, would typical be $\sigma_{\bar{\nu}p} \sim 5 \times 10^{-44}$ cm^2. In 1956 Cowan C.L. Jr, Reines F, Harrison F.B., Kruse H.W. and McGuire A.D. (Fowler 1956) reported detecting neutrinos in the inverse β decay ($\bar{\nu}_e + p \rightarrow n + e^+$) experiment. Until then,

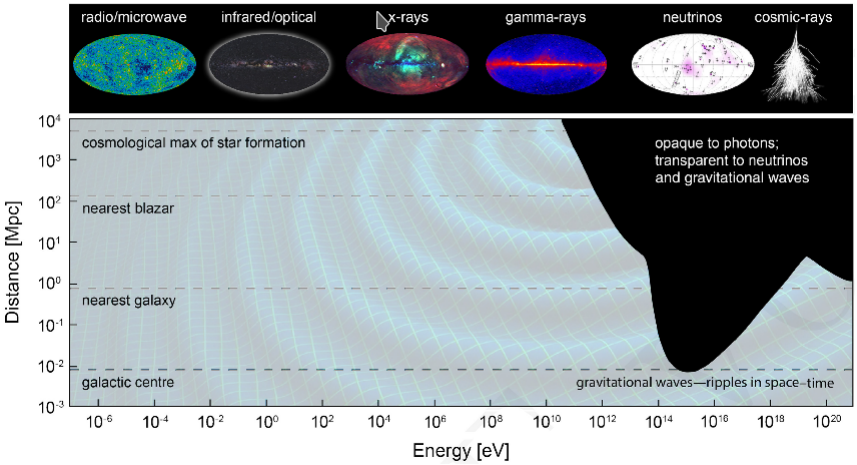

FIGURE 2.1: Lower-energy photons can travel to Earth from the extragalactic distances whereas high energy photons and cosmic rays are attenuated after shorter distances. Therefore, obscuring our view of the most energetic astrophysical events. In contrast, gravitational waves (GW) and neutrinos can travel through the Universe without being attenuated or deflected. Hence, GW and neutrinos make suitable probes of the high-energy sky. Credit: Shawhan 2018

the existence of neutrinos was purely hypothetical.

Neutrino astronomy provides the possibility of observing sources which correspond to the central engines of the most energetic astrophysical phenomena in the Universe. This implies that the inner regions of TDEs can be probed using extragalactic neutrinos tomography[1]. Neutrino astronomy may provide valuable clues for understanding the properties of neutrinos and their interactions at energies in the range $10^{14} - 10^{19}$ eV. At this energy range, we can probe the Universe at a significantly greater distance than is possible with known cosmological sources.

There are three types of neutrinos, also referred to as neutrino flavours. The electron neutrino (ν_e), which accompanies $\beta-$decay. The muon neutrino (ν_μ), which accompanies pion decay, and the tau neutrino (ν_τ), which is only produced in very high energy nuclear reactions. The three flavours of neutrinos all have their anti-particles. Each neutrino flavour will produce a different signature in the detector corresponding to each neutrino flavour (see Figure (2.4)). Neutrino energies depend on the process which forms them. Due to their charge-less nature, there is no way to accelerate neutrinos using an electric field. More energetic neutrinos are more likely to interact and leave traces. They are more likely also to transfer that energy to other particles, that detectors can pick up. Figure (2.2) shows the different cosmological sources with their corresponding neutrino energies and cross-sections. The neutrino cross section,σ, determines how likely an interaction is to occur. Solar neutrinos within the range of 100 keV have a neutrino-nucleon scattering cross section of $\sigma \sim 10^{-45}$ cm^2/nucleon. The interaction probability of the neutrinos with Earth is $\phi = \frac{\sigma d\rho}{<m>}$ cm^2 where $< m >=< A > m_p$ is the average atomic mass of

1. Extragalactic neutrino tomography refers to using neutrinos to study the TDE by imaging the different neutrino producing sites.

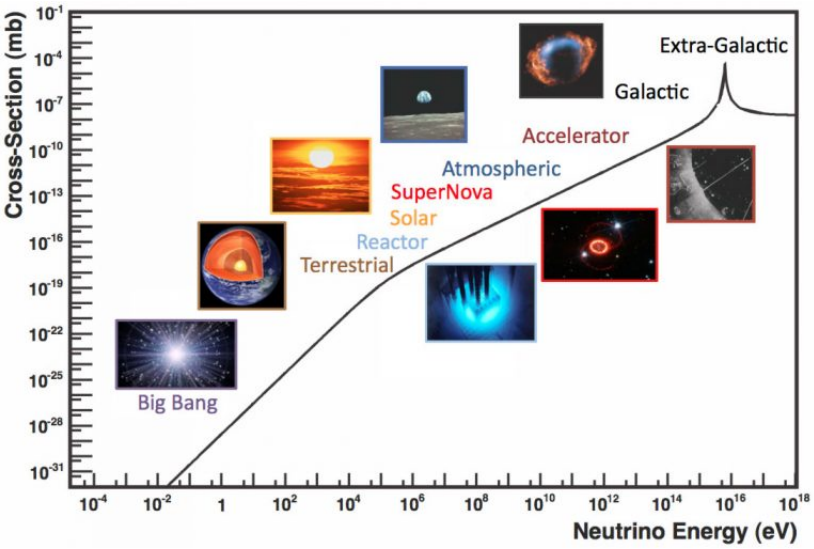

FIGURE 2.2: The relationship between neutrino energies and their cross-section depending on the cosmological source from which they originate. The higher the neutrino energies, the more likely its interaction with regular matter, hence a relatively larger cross-section. The peak at 10^{16} eV is due to the Glashow resonance, which occurs when ultra-high energy electron anti-neutrinos allow the resonant formation of W^- in their interactions with electrons at 6.3 PeV. Credit: Formaggio and Zeller 2012

the Earth, $< A >$ the average atomic number of Earth's material and mp the proton mass.

Neutrinos are characterised by extremely low probabilities of interactions, thus making neutrino physics measurements a difficult feat. In practice, the challenge is twofold. Experiments must rely on huge fluxes travelling through huge detectors, to accumulate enough statistics. The number of interactions is proportional to these two factors. The background noise is difficult to handle due to the scarcity of neutrino bright astrophysical sources; nevertheless, neutrino interactions have been detected from various sources.

Neutrinos of different energy scales are produced in different processes, and diverse astronomical sources are responsible for the total detected neutrino flux. The only confirmed extraterrestrial neutrino sources are the Sun (Davis Jr, Harmer, and Hoffman 1968) and the supernova SN1987A (Burrows and Lattimer 1987) in the nearby Large Magellanic Cloud. The detectors observed roughly 25 neutrino interactions at Kamionkande (Japan) and Baksan (Russia). Neutrinos are the only particles that can penetrate the very dense material produced in a collapsing star.

2.1.1 Neutrino kinematics

If not labeled explicitly all the information of this section are based on Böttcher et al. 2013, Section 3.2. Two processes can produce astrophysical neutrinos, namely nucleon interactions and photonuclear interactions of very high energy (VHE) protons. The efficiency of neutrino production depends on which fraction of their energy protons convert into charged pions. The decay of charged secondary pions

(equation (2.2)) originating from interactions of VHE protons with ambient high-energy photons. A fraction of the kinetic power is converted into the acceleration of relativistic protons. The two main models are distinguished based on $p\gamma$ or pp interactions. Assuming that a significant fraction of the kinetic luminosity within the jet gets converted into the acceleration of relativistic protons and those protons can reach the threshold for $p\gamma-$interactions, synchrotron supported pair cascade may occur (Mannheim and Biermann 1992). Photohadronic $\nu-$production is the result of the decay of charged secondary pions

$$\begin{aligned} \pi^0 &\rightarrow \gamma_1 + \gamma_2 \\ \pi^+ &\rightarrow \mu^+ + \nu_\mu \rightarrow e^+ + \nu_e + \bar{\nu}_\mu + \nu_\mu \\ \pi^- &\rightarrow \mu^- + \bar{\nu_\mu} \rightarrow e^- + \bar{\nu_e} + \nu_\mu + \bar{\nu}_\mu \end{aligned} \tag{2.2}$$

A fraction of the jet kinetic power is converted into the acceleration of relativistic protons; the two main models are distinguished based on $p\gamma$ or pp interactions. Assuming that a significant fraction of the kinetic luminosity within the jet gets converted into the acceleration of relativistic protons and those protons can reach the threshold for $p\gamma-$interactions, synchrotron supported pair cascades may occur (Mannheim and Biermann 1992). In order to accelerate protons to the necessary ultra-relativistic energies (UHE), a high magnetic field of at least several tens of Gauss is required to confine the protons in the emission region.

In astrophysical environments harbouring dense radiation fields with higher photon energies, the particle production threshold can be reached at proton energies of $\sim 10^{16}$ eV. At low interaction energies, the $\Delta^+(1232)-$ resonance [2] dominates the cross-section near threshold (Mucke et al. 1999).

The relativistic electrons provide a synchrotron photon field for high-energy protons. Photopion production is followed by electromagnetic cascade reprocessing the injected power of the pion decay products (Mannheim and Biermann 1992). Only infrared and higher-frequency photons are relevant for photopion production when considering protons with energies above 10^{16} eV.

For the $p\gamma$ interaction scenario, pions are produced in the following reactions;

$$p + \gamma \rightarrow \Delta^+ \rightarrow \begin{cases} \pi^+ + n, & \frac{1}{3}\text{of all cases} \\ \pi^0 + p, & \frac{2}{3}\text{of all cases} \end{cases} \tag{2.3}$$

In certain conditions, the secondary electrons from the pair and photomeson production processes cool mainly through synchrotron radiation. The emission regions are not optically thin to the synchrotron emission from first-generation secondary particles- hence leading to the development of cascades. If all mesons and muons decay with their production energy the flavour ratio of the generated neutrinos would be $\nu_e : \nu_\mu : \nu_\tau \simeq 1 : 2 : 0$ and will oscillate on propagation to Earth to a flavour ratio $\nu_e : \nu_\mu : \nu_\tau \simeq 1 : 1 : 1$ (Becker 2008). This decreases the number of muon tracks but does not necessarily decrease the observability of the source. In the presence of a strong magnetic field, the muons will lose energy due to synchrotron radiation (muon damping) before decay. In that case, the production flavour ratio could be

2. The $\Delta^+(1232)$ resonance is the first excited state of the nucleon. This resonance dominates the pion-production phenomena and plays a crucial role in the physics of the strong interaction.

close to $\nu_e : \nu_\mu : \nu_\tau \simeq 0 : 1 : 0$ (Pakvasa 2008). The detection of ν_e is minimally required for testing neutrino oscillation. The electron neutrinos produced in β-decays have much lower energies in comparison to the muon neutrinos produced through the more energetic pion decay. Measuring the different flavours using neutrino telescopes has proven to be a difficult feat because the showers produced by ν_e and ν_τ look similar.

The relativistic electrons provide a synchrotron photon field for the high-energy protons. Photopion production is followed by electromagnetic cascade reprocessing the injected power of the pion decay products (Mannheim and Biermann 1992). For protons with energies below 10^{16} eV, only the infrared and higher-frequency photons are relevant for photopion production.

In certain conditions, the secondary electrons from the pair- and photomeson production processes cool mainly through synchrotron radiation for which the source may become optically thin. The calculations of the spectra of the secondary electrons are essential because the synchrotron emission of these electrons carries information about the energy spectra of the accelerated protons.

2.2 Relativistic kinematics and cross sections

In this Section, we calculate the energy that a proton requires to undergo photon-proton interactions. Consider relativistic protons with energies $E_p = \gamma m_p$ (we use units with c = 1) and rest mass m_p, which interact with a photon of energy E_{ph} at an angle θ. We are interested in finding the threshold condition for the photopion production process. We assume that the process takes place at the centre-of-momentum (CM) such that the newly produced proton and pion will be at rest in the CM frame. Therefore in the CM frame, the incoming proton would have enough energy per particle to produce the pion in the interaction. The total center of momentum (CM) energy squared $s = m_p^2 c^4 + 2E_{ph}E_p(1 = \beta cos\theta)$.

The energy-momentum conservation dictates that :

$$\bar{P}_{Tot}^{in} \equiv \bar{p}_p^{(in)} + \bar{p}_{ph} \equiv \bar{P}_{Tot}^{out} \equiv \bar{p}_p^{(out)} + \bar{p}_\pi \tag{2.4}$$

with the four-momenta of the produced proton and pion being represented as

$$\bar{p}_{p/\pi} = \gamma_{p/\pi} m_{p/\pi} \begin{pmatrix} 1 \\ \bar{\beta}_{p/\pi} \end{pmatrix} \tag{2.5}$$

We evaluate the four-vector scalar product of $\bar{P}_{Tot}$ with itself:

The left hand side yields

$$(\bar{p}_p^{(in)} + \bar{p}_{ph}) \cdot (\bar{p}_p^{(in)} + \bar{p}_{ph}) = m^2 + 2E_{ph}\gamma_p m_p(1 - \beta cos\theta) \tag{2.6}$$

where $\bar{p}_{ph} \cdot \bar{p}_{ph} = m^2 = 0$ and $\beta = \sqrt{1 - \gamma^{-2}}$.

Evaluating the right-hand side of equation (2.4) in the CM frame at the threshold we obtain

$$(\bar{p}_p^{(out)} + p_\pi) \cdot (\bar{p}_p^{(out)} + p_\pi) = (m_p + m_\pi)^2 \tag{2.7}$$

The head-on-collision ($cos\theta = -1$) is the most favourable case energetically, leading to

$$\gamma_p m_p (1+\beta) = \frac{m_\pi m_p}{2E_{ph}}(2 + \frac{m_\pi}{m_p}) \tag{2.8}$$

Thus the photopion production will only take place if

$$\begin{aligned} E_p^{thr} &\geq \frac{m_\pi m_p}{2E_{ph}}(1 + \frac{m_\pi}{2m_p}) \\ &\simeq 10^{17}[\frac{E_{ph}}{1eV}]^{-1} eV \end{aligned} \tag{2.9}$$

About $\frac{2}{3}$ of the energy lost by protons is inherited by the π^0's and the other $\frac{1}{3}$ goes to the π^+'s . The average pion energy is 20% of the energy of the parent proton. This energy is approximately evenly distributed between the $\pi^\pm$ decay products. Thus, approximately $\frac{3}{4}$ the energy lost by protons of energy E_p is converted to neutrinos with energy, $0.05E_p$.

The $p\gamma-$interactions are dominated by resonance production at low energies. The incoming proton is excited to a baryonic resonance due to the photon being absorbed. The baryonic resonance has very short lifetimes and decays immediately into hadrons. The threshold energy of pion production in the proton's rest frame is $E_{th} = 0.15GeV$. The cross-section for $p + \gamma \rightarrow \Delta^+ \rightarrow \pi^+ + n$ in the proton rest frame depends on the photon E_{ph} (in the proton rest frame as well).

The most important resonance in the photopion production channel is the $\Delta^+(1232)$ (also referred to as the '$\Delta-$approximation') resonance with $m_{\Delta^+(1232)} = 1.232\,\mathrm{GeV/c^2}$ and $\Gamma_{\Delta^+(1232)} = 0.511$ GeV being the resonance mass and Lorentzian width, respectively. This resonance has been used to construct approximate pion production cross section near the threshold. The more massive resonances also contribute to the photopion production. The $\Delta-$resonance is called the isospin $\frac{3}{2}$ and N resonances are called isospin $\frac{1}{2}$ particles. Baryonic resonances in $p\gamma-$reactions include the $N^+(1440)$, $N^+(1535)$, $N^+(1520)$, $N^+(1650)$, $N^+(1680)$, $N^+(1950)$, $N^+(1700)$ and $N^+(1905)$. N and Δ denote the resonance with isopin $\frac{1}{2}$ and $\frac{3}{2}$, respectively. While the plus sign represents the charge of the resonance and the bracketed number is the nominal mass.

The $\Delta^+(1232)$-resonance (Stecker 1973) has the highest cross section at low interaction energies while the direct channel dominates near threshold. The direct channel can be crucial for proton interactions in soft photon spectra because it exclusively produces charged pions. The $\Delta^+(1232)$-resonance is the first excited state of the nucleon (proton or neutron) with a mass of $m_{\Delta^+(1232)} = 1.232\ \mathrm{GeV/c^2}$ and a corresponding half-life of $\sim 3.87 \times 10^{-24}s$. In the $\Delta-$approximation (Stecker 1973), as described by Mucke et al. 1999, the cross section is given as

$$\sigma_\Delta = 500\mu barn\theta(\sqrt{s} - m_\Delta + \Gamma_{\Delta/2}) \cdot \theta(m_\Delta + \Gamma_{\Delta/2} - \sqrt{s}) \tag{2.10}$$

where $\Gamma_\Delta = 0.115$ GeV is the width of $\Delta^+(1232)$, and θ is the Heaviside step function. The $\Delta-$approximation uses the branching ratios of the $\Delta^+(1232)-$resonance to determine the number ratio π^0 to π^+ of $2:1$. The cross-section of the $p\gamma-$interaction process close to the threshold is $\sigma_{p\gamma} \simeq 6 \times 10^{-28}$ cm ^{2} and drops to $\sigma_{p\gamma} \simeq 10^{-28}$ cm ^{2} above the threshold energies. The average fractional energy of a proton going to a pion is 0.2.

2.3 Neutrino detection

The low interaction probability and small neutrino fluxes of VHE neutrinos above the TeV energy range require large detector volumes. The whole detector volume has to be instrumented to be able to record the interactions of neutrinos and the energy loss of the muons. It is crucial to construct a simple and cost-effective detector. The only candidates which meet these conditions are huge water and/or ice Cherenkov counters.

The Cherenkov effect occurs when coherent emission of light follows a characteristic angle by the Mach relation

$$cos\theta = \frac{1}{\beta n} \tag{2.11}$$

where β is the speed of the particle tranversing the medium in units of the speed of light and n is the index of refraction of the medium. The Cherenkov effect takes place when

$$\beta > \frac{1}{n(H_20)} \tag{2.12}$$

this was first posited by Heaviside and Vavilov where as Cherenkov. Charged particles which obey Equation (2.12) will be detected by the Cherenkov detector. This gives a threshold energy per particle of $\sim$ 0.8 MeV for electrons, 160 MeV for muons as well as 1.4 GeV for protons and neutrons. The Cherenkov radiation accounts for a small fraction of the total energy loss of a charged particles traveling through a medium.

In water Cherenkov detectors, the Cherenkov radiation is detected, and the cone of emission is reconstructed. The axis of the cone gives the direction of the particle, and the light which is produced is a measure of the neutrino energy. Neutrino detectors are made-up of large arrays of photomultipliers which record the Cherenkov light of muons produced in water or ice. The photomultipliers are placed at a distance depending on the absorption and scattering length of Cherenkov light in the medium. In a water Cherenkov detector, the ocean's bioluminescence and potassium-40 produce background noise hindering the detections. This is not present in ice detectors.

In Cherenkov detectors, the Earth is used as an absorber to protect the detector against the relatively high flux of atmospheric particles. So neutrinos which enter the detector "from below" are only considered. The Cherenkov light emitted by down-going leptons, i.e. leptons travelling from the Earth to the bottom of the sea is regarded as background and these do not point back to a neutrino. This background serves as a standard calibration source. Upward moving leptons are formed when a neutrino undergoes a charged current (CC) interaction with a nucleon below the detector. Electrons lose their energy too fast and the tau decay too fast, thus both leave short tracks whereas muons leave the longest trail in the detector (Bouwhuis 2005). Consequently, from the upwards travelling leptons, muons are the easiest to reconstruct. These upward travelling muons can originate from a cosmic neutrino or an atmospheric neutrino. The discrepancy between these two can be seen from the energy distribution of the measured neutrinos. The atmospheric neutrino spectrum is known, so the cosmic neutrino spectrum can be extracted after

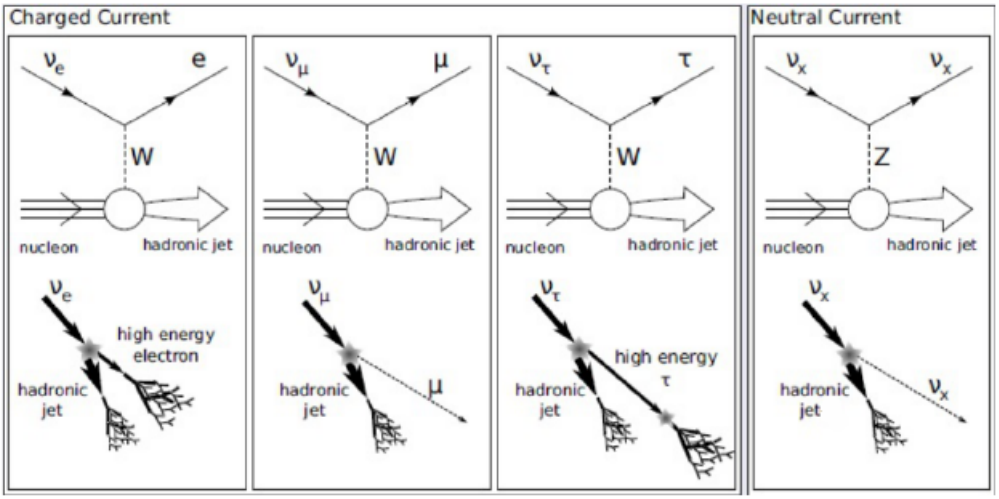

FIGURE 2.3: The Feynman diagrams showing the high-energy neutrino interactions of neutral current (NC) and charged current (CC). Credit: Abreu et al. 2011

subtracting the atmospheric neutrino spectrum from the total detected neutrino flux spectrum. Muons have a large mean free path in matter; hence, deep underwater ice Cherenkov detectors are more efficient in detecting muons from $\nu_\mu \rightarrow \mu$ conversions. Atmospheric neutrinos are isotropically distributed along the sky, so focusing on a known location along the sky will reduce the background atmospheric neutrino/ noise. This approach requires good statistics and accurate energy reconstruction. Another neutrino-search approach is called the background discrimination. This is takes place when a particular location of the sky is searched for muons.

Neutrinos are detected in water Cherenkov when they interact by W exchange, converting into the equivalent charged lepton (muon or electron for ν_μ or ν_e respectively), or when they elastically scatter off electrons (when the recoil electron can be detected). Identifying ν_τ is more difficult, because of the short lifetime of the tau. The interaction between high energy neutrinos ($E_\nu \simeq 100$ GeV) and matter occurs predominantly through the deep-inelastic scattering of nucleons. The neutrino scatters off quarks in the target nucleus by the exchange of a Z or W weak boson known as a neutral current (NC) interactions

$$\nu_l + N \rightarrow \nu_l + N, \tag{2.13}$$

and charged current (CC) interaction

$$\nu_l + N \rightarrow l + X \tag{2.14}$$

The NC interaction leaves the neutrino state intact, while for the CC interaction, a charged lepton is produced, which shares the initial neutrino flavour (see Figure (2.3)). Different methods are used to detect the high energy secondary particles created in CC and NC neutrino interactions. Cherenkov detectors observe the radiation of optical Cherenkov light given off by secondary charged particles produced in CC and NC interactions that travel faster than the speed of light in the medium.

The principle classes of Cherenkov events are identified by "tracks" and "cascades" as described in Figure (2.4). Tracks are Cherenkov emission of long-lived

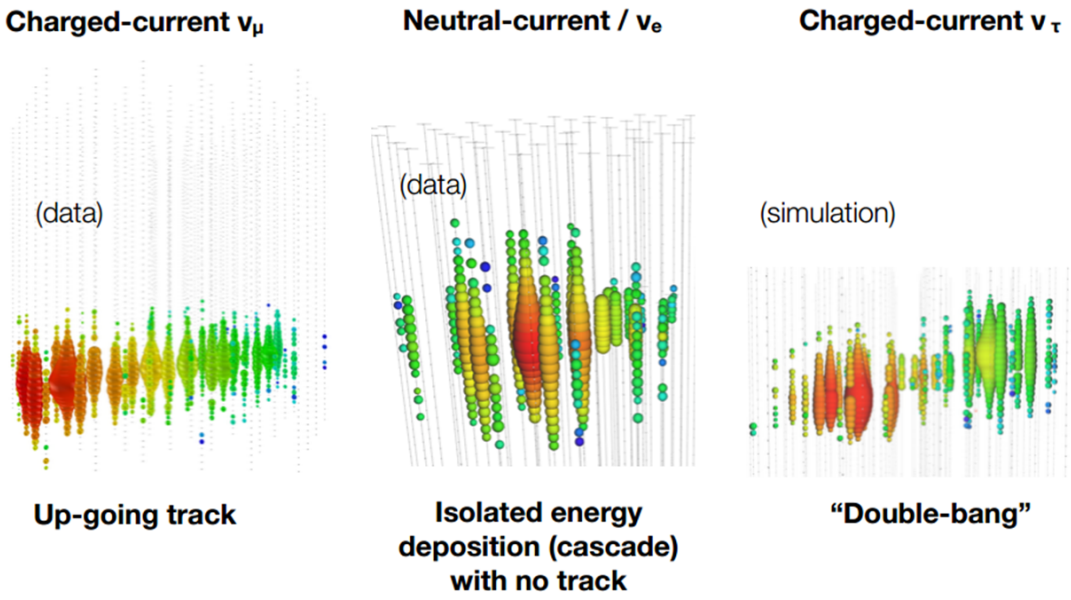

FIGURE 2.4: These are the different event signatures in the detector. Neutral current and charged current interactions involving ν_e produce a cascade-like signature. Events forming due to charged current interactions of ν_μ are represented by track-like signatures, whereas the ν_τ charge current interactions have a "double bang" signature. Credit : Madsen 2019

muons passing through the detector. These muons may be produced in CC interactions of muon neutrinos inside or in the vicinity of the detectors. The cascade events occur when the hadronic particle shower generated by the target struck by a neutrino in the ice also radiates Cherenkov photons, leading to a large multiplicity of secondary particles and the repeated scattering of the Cherenkov photons in the medium. This light pattern is mostly spherical. The Cherenkov emission of secondary particles close to the neutrino interaction point helps to reconstruct the direction of the initial neutrino, whereas the angular resolution becomes much worse than for the track events. However, cascade events allow for a better energy resolution because the Cherenkov light is proportional to the energy transferred to the cascade, which is fully contained in the instrumented volume.

The number of neutrinos one may expect in a detector is proportional to the neutrino flux, the cross-section of the neutrino interaction and the number of target atoms/molecules in the detector. Hence, it is vital to know the neutrino cross-section to estimate the number of neutrino interactions one may expect in the detector.

These searches enable higher statistics at the expense of greater atmospheric background. However, spatial coincidence with a potential source significantly decreases the background noise for a search. Astrophysical neutrino sources are expected to have a harder spectrum in comparison to the background atmospheric neutrino flux. Considering temporal coincidence, i.e. lifetime of a transient, or the duration of 'interesting flaring periods' could also prove to be an advantageous approach to reduce the noise. Alternatively, the neutrino-driven approach entails selecting neutrino events which have a high probability of originating from astrophysical sources, which is determined by their reconstructed topology and energy.

This approach forms the basis of the IceCube Realtime Program (Aartsen et al. 2017) aimed at identifying astrophysical neutrinos in real-time and immediately alerting astronomers through the Gamma-ray Coordination Network (GCN) framework. The high-energy neutrino, IC170922A, is the most successful neutrino-driven approach so far. This detection launched a comprehensive, multi-messenger follow-up campaign.

2.4 Tidal disruption events

Supermassive black holes (SMBHs) are known to reside in the centre of most galaxies, including Sagittarius A* in our Milky Way. These SMBHs are responsible for the evolution and growth of their host galaxies. The tidal disruptions and accretion of stars may in turn fuel these SMBHs in the centres of galaxies (Hills 1975). Additionally their contribution to nuclear activities in galaxies and the growth of the SMBH mass depends on the rate of disruption events in a galaxy. Galaxy mergers have been suggested, through observational and theoretical simulations, to enhance TDE rates. In this section we will explore the physics of TDEs. Large parts of the text are based on the work of Stone 2014, in particular Section 1.1.3 therein.

The theorist John A. Wheeler 1971 suggested that the disintegration of a star in the ergosphere of a rotating BH could induce the acceleration of the released gas particles to relativistic speeds. The basic framework of these transient episodes considers a BH embedded in a spherically symmetric cluster of stars whose velocities are isotropically distributed. Stellar dynamics in galactic nuclei are collisional, over long timescales. The orbital characteristics of individual stars change as a result of perturbations from tidal/gravitational interactions between stars or other astrophysical objects such as compact stellar remnants, or more massive objects. Infrequently, the trajectory of a star can be perturbed, subsequently passing so close to the central SMBH that it will be partially or completely shredded by the tidal forces (Hills 1975; Rees 1988). The fallback stellar debris will create a transient accretion disk, which will then launch a luminous high-energy flare. Most tidally disrupted stars are assumed to come from large radii and need to reach pericentre at $\sim 50R_g$ where $R_g = \frac{GM_{BH}}{c^2}$ is the gravitational radius, resulting in an eccentricity of the orbit as close to unity: e = 1.The transient multiwavelength flare produced by the TDE has supernova-like luminosities, and their associated relativistic jets are visible over cosmological distance. The current accepted TDE model was established in the late 1980's by Rees 1988, Phinney 1989 and Evans and Kochanek 1989. The flares are said to carry information on the make up of the star and the physics of the SMBH. A possible argument stems from the fact that knowledge of the energetics and dynamics of the TDEs may revel the star's binding energy and the dynamics which governed the SMBH prior to the disruption.

SMBHs are highly relativistic; therefore, general relativity (GR) effects do play a role in the dynamics of TDEs. In this work, we will only discuss the Newtonian picture, for a more detailed approach on the role of GR in TDEs (see Stone and Loeb 2012).

TDE rate which is expected in a single galaxy is,

$$\Gamma_{TDE} \sim \Gamma_{loss} \sim 10^{-4} yr^{-1} \left(\frac{M_{BH}}{M_\odot}\right)^{\frac{4}{3}} \left(\frac{N_*}{10^5 pc^{-3}}\right) \left(\frac{\sigma}{100 km.s^{-1}}\right)^{-1} \tag{2.15}$$

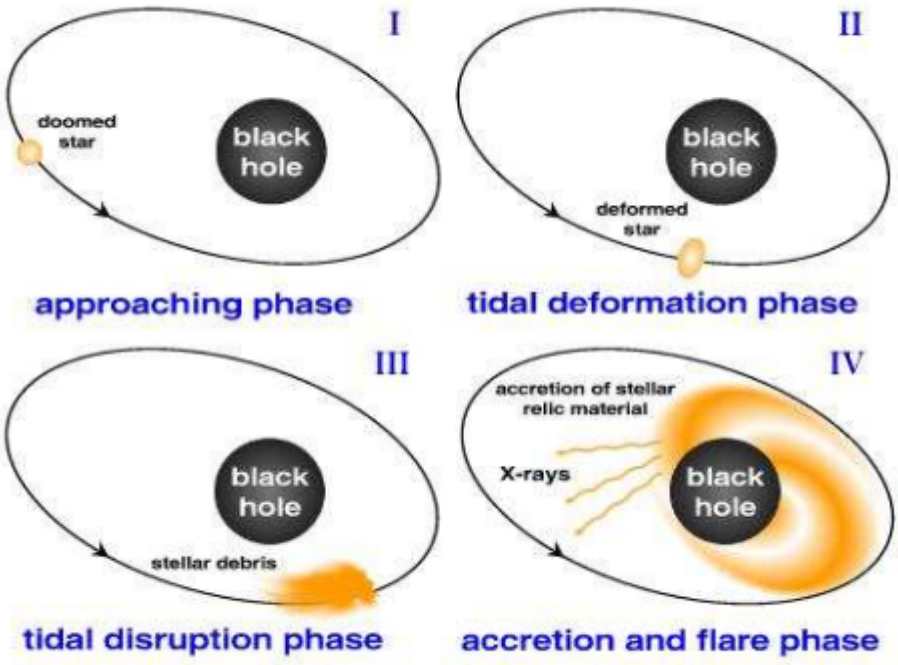

FIGURE 2.5: (I)When a star with mass, M_*, and radius, R_*, approaches a SMBH of mass, M_{BH}. (II) In the event of a star being disrupted, approximately half of the stellar debris will be bound to the SMBH (orange). (III) The more bound matter could accrete onto the black hole (BH), although there is a prospect that shocks from returning material could unbind some of the matter. Credit: Müller (2007)

where N_* and σ_* are the stellar number density star cluster. The total TDE rate is obtained by a convolution of the Equation (2.15) with the number density of galaxies in the local Universe and the BH mass function.

2.4.1 The Newtonian picture

When a star of mass M_* and radius R_*, get spawn into an orbit around a SMBH of mass M_{BH} with an orbital pericentre distance, r_p, which is less than the tidal radius

$$r_t = R_*(\frac{M_{BH}}{M_*})^{\frac{1}{3}}. \tag{2.16}$$

$$\sim 7 \times 10^{12}(\frac{R_*}{R_\odot})(\frac{M_*}{M_\odot})^{-\frac{1}{3}}(\frac{M_{BH}}{10^6 M_\odot})^{\frac{1}{3}} \text{ cm} \tag{2.17}$$

a TDE occurs. This scenario, $r_p < r_t$, is the mathematical representation of the tidal disruption phase seen in Figure (2.5). The tidal radius refers to the distance at which the star is disrupted. In reality, the tidal radius may also depend on the stellar structure, stellar spin and BH spin. The tidal disruption radius is a critical distance at which a star can be disrupted. The strength of the disruption event is determined by the dimensionless impact parameter

$$\beta = \frac{r_t}{r_p} \tag{2.18}$$

which measures the strength of the tidal encounter. In this study, we only focus on jetted TDEs, which occur during total stellar disruption. These TDEs produce relativistic X-ray bright jets (Shen and Matzner 2014). For such an event to be detectable, it needs to happen outside the event horizon of the BH, which is twice the gravitational radius, for a Schwarzchild BH. The criterion which describes a total stellar disruption is given by; $1 < \beta < \frac{r_t}{R_s}$ with $R_s = \frac{2GM_{BH}}{c^2}$ representing the Schwarzschild radius. Any star that ventures beyond this distance,$\beta > 1$, will get caught in the potential well of a BH and eventually get tidally disrupted. A star will only be partially disrupted if $\beta < 1$ whereas if $\beta \ll 1$ no disruption will occur.

The horizon of a non-spinning BH grows linearly with M_{BH}, i.e. $R_s \propto M_{BH}$, while the tidal radius only grows as $M_{BH}^{\frac{1}{3}}$, above the Hills mass,

$$M_{Hills} = 1.1 \times 10^8 M_\odot r_*^{\frac{3}{2}} M_*^{-\frac{1}{2}} \tag{2.19}$$

stars will get engulfed by the horizon prior to the tidal disruption (see Figure (2.4.1)). The event horizon of an SMBH of mass $\sim 10^8 M_\odot$ is enclosed in the tidal radius. So, a TDE around such a SMBH can not be observed. The inclusion of relativistic effects may increase this limit to $\sim 10^9 M_\odot$ (Kesden 2012). An example of such a case is ASASSN-15lh, which is a TDE candidate with a suggested BH mass of $\sim 10^8 M_\odot$. Leloudas et al. 2016 suggested that the BH must be spinning therefore making it detectable. TDEs with smaller pericenters will have higher peak luminosities than those with $r_p \sim r_t$. Additionally, considering relativistic effects such as the BH spin may raise the tidal radius limit (Beloborodov et al. 1992). This is because the BH spin becomes important only in the deepest disruption, $R_* > r_p$. SMBHs with masses below $\sim 10^5 M_\odot$ can tidally disrupt white dwarf stars, in this case the TDE would be expected to be a gravitational-source candidate .

The total energy budget for a TDE is set as approximately half of the mass of the disrupted star becomes bound to the SMBH and then eventually accretes onto the BH,

$$E_{max} \sim \frac{1}{2} M_* c^2 \tag{2.20}$$
$$\sim 10^{54} erg, \tag{2.21}$$

for a solar-type mass star (Dai and Fang 2017 andLunardini and Winter 2017). When a star is disrupted a relativistic jet may be launched. These jets consist of gases, with a range of energies. This range of energies occur because some of the stellar debris is deeper in the potential well of the SMBH than other trailing portions.

When the star's gravitational binding energy is exceeded by tidal forces, the star's fluid elements begin to move on roughly geodesic trajectories. If the hydrodynamic forces are neglected the orbital energy, ϵ, of the debris stream with an energy spread given by

$$\Delta\epsilon \simeq k \frac{G M_{BH} r_*}{r_p^2} \tag{2.22}$$

where k is a constant of order unity related to stellar structure and rotation prior to disruption. Equation (2.22) can be obtained by Taylor expanding the SMBH potential around the star at pericentre. Another approach is to multiply the equivalent tidal acceleration at pericentre $a_p \sim (\frac{G M_{BH}}{r_p^2})(\frac{r_*}{r_p})$ by dynamical time $t_p \sim (\frac{G M_{BH}}{r_p^3})^{\frac{-1}{2}}$. The pericentre velocity is given as $v_p = (\frac{2 G M_{BH}}{r_p})^{\frac{1}{2}}$ and assuming that the impulsive delta-v at pericentre $\Delta v_p = a_p t_p$ one can find that $\Delta\epsilon = v_p \Delta v_p \sim \frac{G M_{BH} r_*}{r_p^2}$. Once the star reaches the pericentre distance, the star becomes highly non-spherical due to the tidal stretching. Consequently the fluid elements move along geodesic trajectories with a large velocity shear. Thus the differential energy between the two fluid elements will depend on their individual positions and velocities.

In the early stages of a disruption, before the star arrives at the pericentre, motions orthogonal to the orbital plane will separate from the motion within the pericentre radius. This leads to a strong one-dimensional compression of the star. This compression is reversed by the internal pressure generated in the disruption, which leads to a rebound in the vertical direction. This rebound is accompanied by shock formation. The distortion imparts a range of mechanical energies $\varepsilon \sim [-\epsilon, +\epsilon]$. If $\varepsilon < 0$ is bound to the SMBH and $\varepsilon > 0$ escapes to infinity.

The canonical TDE model assumes that the bolometric luminosity of a TDE is proportional to the fallback rate,

$$L(t) = \eta \dot{M}(t) c^2 \tag{2.23}$$

where η is a radiative efficiency and $\dot{M}$ is the mass accretion rate. For a flat energy distribution over $[-\epsilon, +\epsilon]$,

$$L(t) \sim 3 \times 10^{11} L_\odot (\frac{\eta}{0.1})(\frac{M_{BH}}{10^6 M_\odot})^{\frac{1}{6}} (\frac{t}{t_0})^{\frac{-5}{3}} \tag{2.24}$$

where t_0 is the minimal orbital period of bound debris.

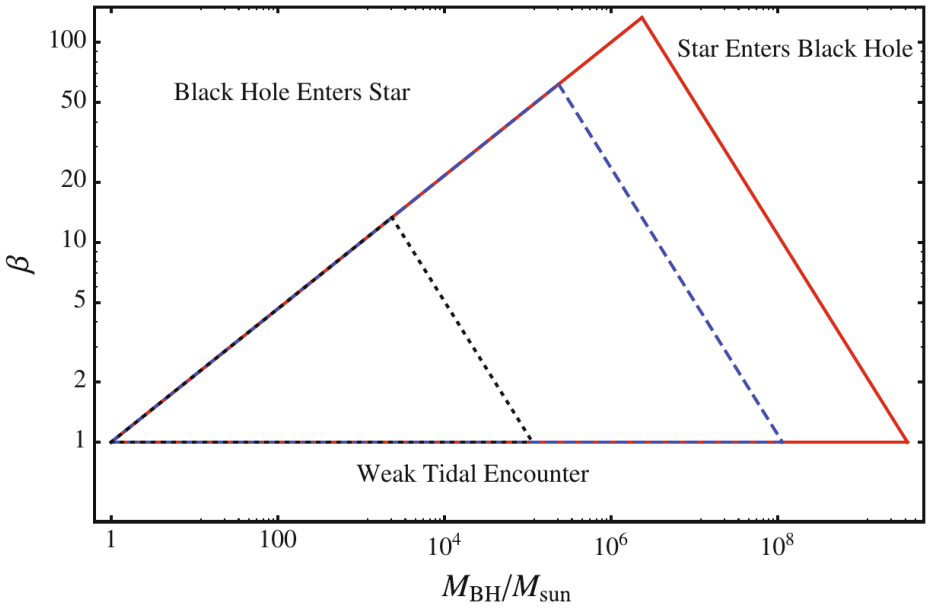

FIGURE 2.6: The parameter space of a tidal disruption within the Newtonian regime. These three triangles represent solar-type stars (blue, dashed) red giants with $M_* = M_\odot$, $R_* = 10R_\odot$ (red, solid), and white dwarfs with $M_* = M_\odot$, $R_* = 10^{-2}R_\odot$ (black, dotted). Only stars in their respective triangles may undergo a tidal disruption. When $\beta < 1$ the tidal encounters are only partial disruptions implying that mass is partially stripped from the star, this occurs in the area below the triangle . If the stars encounter a BH which is larger than its Hills mass limit (equation (2.19)) then the star will be swallowed whole.This will happen if and only if the star is within the upper right corner. The upper left corner describes engulfment of small BH by a star. White dwarfs, solar-type stars and red giants may reach maximum β values 13, 62 and 133, respectively.
Credit : Stone 2014

The observable characteristics of a TDE is determined by the evolution of the stellar debris following the disruption. Hence, one may ask "Which component of the debris may dominate a TDE event's energy output : the bound or unbound debris?".

X-ray bright jetted TDEs [3] show luminous thermal optical emission (Pasham et al. 2015), most of the optical and soft X-ray detected flares are radio-quiet (Bower et al. 2013). The X-ray flares have a typical signature such as thermal radiation; the X-ray luminosity decays with time according to a power law, $L_X \propto t^{-\frac{5}{3}}$ with typical timescales of months. It is unclear why this timescale declines with at this trend (Ageron et al. 2011). The observation of a stellar tidal disruption of a solar-type star immediately constrains the BH mass smaller than $\sim 10^8 M_\odot$ because larger BHs the tidal radius is smaller than the Schwarzschild radius (Hills 1975). The first TDEs were detected in soft X-rays, however many optically discovered events produce no detectable X-ray emission (e.g. PS1-10jh, Gezari et al. 2015 and ASAS-SN14ae Holoien et al. 2014) or do so only after a significant delay e.g. D3-13 (Gezari et al. 2006) and D1-9 (Gezari et al. 2015). These jets are likely to have successful jets with an isotropic equivalent luminosity, $L \gtrsim 10^{44.5}$ erg·s^{-1} (Senno, Murase, and Mészáros 2017). As mentioned above, we focus on jetted TDEs. Another species of TDEs are hydrodynamically choked TDEs. The major difference, as the name suggests, lies in their jet launching inabilities. Choked TDEs may potentially also produce VHE neutrinos. TDE with weaker jets might also be Compton dragged to low Lorentz factors resulting in the $\gamma-$ray emission being strongly suppressed. The high optical depth of the UV photosphere of TDEs curtails the gamma rays.

Farrar and Piran 2014 showed that jetted TDEs met all the necessary criteria to accelerate protons to energies $E \sim 10^{20}$ eV and might be abundant enough to account for the observed ultra high energy neutrino flux. Protons may be accelerated by shocks as they propagate through the jet. This interaction may also produce neutrinos when the protons interact with the surrounding dense photon fields. Fermi-LAT data show no $\gamma-$ray emission for Swift J2058, Swift J1112-8238, Swift J1644+57 and AT2019dsg; thus, TDE jets are gamma ray-dark neutrino sources towards GeV-TeV $\gamma-$rays. This indicates that this emitting region might not be transparent to $\gamma-$rays i.e. $\tau_{\gamma\gamma}(E_\nu \geq 100 \text{ MeV}) > 1$. This may help in placing an upper limit on the bulk Lorentz factor (Peng, Tang, and Wang 2016).

TDEs are expected to be fairly common in neighbouring galaxies, occurring at least once every $\sim 10^4$years in a galaxy similar to the Milky Way. A few candidate TDEs have been identified through the soft X-ray thermal spectra predicted to characterize their accretion disks and their characteristic light curves, which peak days to months after the disruption.

To date the Open TDE Catalog[4] currently lists $\sim$ 100 TDE candidates. In the near future, this catalogue is most likely to increase due to detections by ongoing surveys such as the Zwicky Transient Facility (ZTF), (Graham et al. 2019) and other upcoming surveys, e.g., the eROSITA All-Sky Survey (Merloni et al. 2012) and the Large Synoptic Survey Telescope (LSST, Ivezic et al. 2009). One of the best observed TDEs is Swift J1644+57. Others include Swift J2058.4+0516, Swift J1112.2-8238 and

3. jetted TDEs, those characterized by non-thermal X-ray and synchrotron radio emission.
4. https://tde.space/

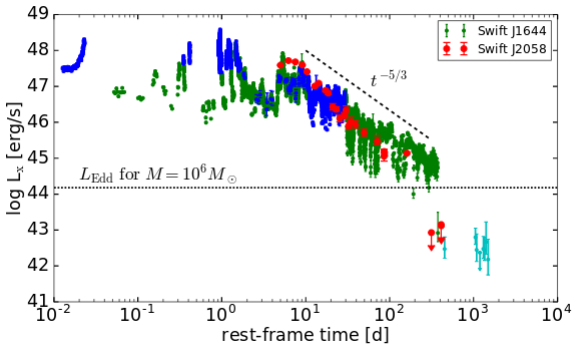

FIGURE 2.7: A light curve of two jetted TDEs Swift J1644+57 (blue, green and cyan) and Swift J2058 (red). The dashed line shows the X-ray emission dropped roughly as $t^{\frac{-5}{3}}$ for both TDEs. Swift J1644+57 shows many dips at different timescales accompanied by a relatively flat trend for ten days followed by intense flares with a variability timescale of $\sim$ 100 s. After approximately 500 days there is a sudden drop in the X-ray emission likely due to the relativistic jet being switched off (Zauderer et al. 2013).

AT2019dsg. These four TDEs are all observed to launch jets.

2.4.2 Observations of Swift J1644+57

Swift J1644+57 was first detected when it triggered the Swift Burst Alert Telescope (BAT) on the 28^{th} of March 2011 12:57:45 UT (Burrows et al. 2011) and initially shared similarities with previously detected GRBs. However, the X-ray emission did not fade as quickly as expected for GRBs. The rapid rise, huge X-ray peak luminosity, long duration, compact and variable associated radio emission, and optically inactive host galaxy all contributed to the interpretation of this event as the launch of a powerful jet following the tidal disruption of a star (Bloom et al. 2011, Burrows et al. 2011, Zauderer et al. 2011,Levan et al. 2011). TDEs are by nature nuclear transients. The flares may sometimes be mistaken as GRBs and AGNs. The source is a broadband emitter, emitting photons from radio to hard X-rays. The early evolution of the light curve is characterized by an isotropic peak luminosity of $L_X \simeq 4.3 \times 10^{48}$ erg$\cdot$s^{-1} (Burrows et al. 2011). After the first few days, the light curve showed an overall decline to $L_X \simeq 2.96 \times 10^{47}$ erg$\cdot$s^{-1} in the $0.3 - 13.5$ keV band over a time $\Delta t \sim 10^6$s but continues to be highly variable with timescales as short as $t \sim$ 100s. Hence, the internal shocks may occur at a radius $R \simeq 2\Gamma^2 c t_{100s} = 6 \times 10^{10} \Gamma^2 t_{100s}$ cm . The observed radio afterglow of Swift J1644+57 indicates that given a total energy budget of 10^{54} erg (equation (2.21)) the total kinetic jet energy is $\sim 10^{53}$ erg (De Colle and Lu 2019). This is because typically for magnetically driven jets approximately 10% of the accreted energy is carried through the jet. Optical imaging and spectroscopy revealed that the host galaxy is at redshift $z = 0.354$ (Levan et al. 2011). Numerous estimates of the SMBH mass, based on scaling relations or the most rapid variability timescale all give $M_{BH} < 10^7 M_\odot$ (Komossa and Merritt 2008).

TDE flares have been observed at hard X-ray energy band by (Bloom et al. 2011,Burrows et al. 2011,Cenko et al. 2012, Pasham et al. 2015) and in the soft X-ray energy

band by (Bade, Komossa, and Dahlem 1996, Grupe, Thomas, and Leighly 1999,Komossa and Greiner 1999). X-ray emissions have shown evidence for a quasi-periodicity of $\sim$ 200s (Reis et al. 2012,Komossa 2012). The relativistic jet physics of TDEs is dominated by X-ray emissions as a result of forward shocks in the jet. Contrary to the long-term X-ray light curve, the radio emission from Swift J1644+57 continued to rise (Zauderer et al. 2013) to $\sim$ 600 days. Figure (2.7) illustrates the Swift X-ray light curve of Swift J1644+57 which shows a sudden drop at $\sim$ 500 days. Swift J1644+57 lacked detectable UV and optical emission. The high degree of polarization observed in the near infrared was attributed to jetted emission from forward shocks (Wiersema et al. 2012) in the jet and not from the accretion disk. Flares in the UV and optical band have been discussed by Stern et al. 2004, Gezari et al. 2006) and Cenko et al. 2012, Holoien et al. 2014, respectively. The source is located within 150 pc of the centre of a compact galaxy (Levan et al. 2011). Variable emission was also detected in the near-infrared, not in the optical, probably because of the excess extinction seen in the optical spectrum. The rapid decline is not seen in the radio, suggesting that X-ray and radio emission have different sites of origin. Zauderer et al. 2013 postulated that the decline in X-ray emission could have been the result of a change in accretion mode, which leads to the jet production turning off. Consequently, the faint late X-ray stage and the ongoing radio emission are consistent with an increase in the number of relativistic particles from forward shocks in the jet. The X-ray flux of Swift J1644+57 dropped by several orders of magnitude within $\sim$ 1 yr after the peak. This might have been because the stellar material supply dropped with time. The accretion rate drops from super-Eddington to sub-Eddington in the TDE, implying that the accretion disk changes from geometrically thick disc to a thin disc. The jet switches off when the disk becomes optically thin (Tchekhovskoy et al. 2013). The source is still observable (Eftekhari et al. 2018) and becomes non-relativistic at $\sim$ 700 days. Recent observations of Swift J1644+57 were taken in radio (VLA) and X-rays (Chandra) at day 2493 and day 2795.

2.4.3 Magnetic fields in TDEs

An essential question that has emerged (initially in Bloom et al. 2011) is the role of magnetic fields in magnetohydrodynamic jet formation models. The headlining question is whether the required large-scale magnetic field is generated in situ in the disk or is rather advected in with the flow. The estimated magnetic field strength for Swift J1644+57 is much lower than that expected for a main sequence star disruption; hence it might have been generated locally in the disk or is a result of the presence of a fossil disk. The source of the long-term radio emission has been by all accounts described as a consequence of synchrotron radiation from the shock which is formed when the jet interacts with the interstellar medium. Another eminent question has been the nature of the X-ray emission and its rapid variability and early epochs of high amplitude flaring. Several models have associated it with dissipation in the inner jet.The trajectory and type of the disrupted star play a crucial role in terms of the dynamics of the TDE. Substantial studies have explored the disruption of a main-sequence star, different authors have also suggested also recommended the disruption of a white dwarf (Krolik and Piran 2012), a giant star (Shao et al. 2011) or a star with a deeply plunging orbit (Cannizzo, Troja, and Lodato 2011).

Magnetic fields play a crucial role in both the jet launching and collimation. Moreover, they play an important role in particle acceleration and thus flaring of

the TDE. After the disruption of a star, the stellar debris evolves into an extended stream of gas made-up of a bound part that falls back toward the disruption site and the unbound part which escapes the black hole's gravity (Rees 1988). TDEs are thought to inherit magnetic fields from the tidally disrupted star. The bound part can be accelerated and turn into an accretion disk by the magnetic stresses within the stream. Even so, in the case of Swift J1644+57, the stellar magnetic flux is too small to launch a jet powerful enough to account for the measured X-ray luminosity (Piran, Sądowski, and Tchekhovskoy 2015). Alternate theories include an in situ dynamo process creating regions of large magnetic flux within jet (Piran et al. 2015), the disruption of a strongly magnetized star resulting from a recent binary merger (Mandel and Levin 2015). Another possibility is that TDE jets may be radiatively powered (Gezari et al. 2015, Kara et al. 2016, Stone and Metzger 2015). In this case, a large magnetic flux would not be necessary.

In 1969, Penrose discussed how a spinning BH has free energy that may be tapped into. Consequently, this leads to the idea that the energy source behind relativistic jets might be the rotational energy from the accretion of a BH. The extraction of angular momentum powers the outgoing flux. Two theories that may explain how energy can be transformed from a BH into an astrophysical jet are the Blandford-Znajek process (Blandford and Znajek 1977) and the Penrose mechanism (Penrose 1969). The latter occurs when energy is extracted from a rotating BH by frame dragging. A necessary ingredient for this mechanism is a large-scale magnetic field threading the BH. The field lines twist around the BH rotation, as they unwind and expand, plasma gets ejected at relativistic velocities along the direction of the BH spin.

2.4.4 The role of the accretion flow

Accretion occurs when matter falls into a central engine i.e. SMBH, converting gravitational potential energy into radiation. A large fraction of the energy will be lost to the BH while the remainder of the energy heats up due to friction in the accretion disk around the BH. The maximum energy gained for accretion onto a BH, is $E_{max} \sim \frac{GmM_{BH}}{R_s}$ where $R_s = \frac{2GM}{c^2}$. Assuming a spherically symmetric constant accretion flow, the accretion rate is given as

$$\dot{M} = 4\pi r^2 \rho v \tag{2.25}$$

where ρ is the density of the in-falling matter, v is the velocity of the matter and r is the distance from the BH also know. Assuming that the accretion capture radius is correlated to the escaping velocity, v, of a particle at a distance $r = \frac{2GM_{BH}}{V^2}$, then the accretion rate becomes

$$\dot{M} = \frac{4\pi\rho G^2 M_{BH}^2}{v^3} \tag{2.26}$$

The radiation pressure generated by the in-falling matter limits the accretion onto the SMBH. The luminosity from the accretion is

$$L = \frac{\epsilon c^2 \dot{M}}{2} \tag{2.27}$$

where ϵ represents the radiative efficiency.

An astrophysical BH is described by two parameters that effectively set the inner boundary condition for accretion. The BH mass, M_{BH}, determines the characteristic length and time scales close to the horizon, whereas the Kerr spin parameter $\frac{a}{M_{BH}}$ (where $a = \frac{J}{M}$ is the specific angular momentum of the BH, in geometric units G=c=1 with J being the angular momentum of the BH) with $0 \leq \frac{a}{M_{BH}} \leq 1$, determines the efficiency of the energy released. This energy is coupled to the magnetic and radiative properties of the infalling gas. Although the horizon marks the point of invisibility and no return for the matter being accreted by a BH, the energy efficiency of accretion is determined somewhat further out near the innermost stable circular orbit (ISCO). A test particle orbiting inside this radius will be swallowed by the BH infall. The infall is so fast that energy release becomes inefficient. The ISCO radius, R_{ISCO}, decreases from $6M_{BH}(= 3R_s)$ for a Schwarzschild BH (Jefremov, Tsupko, and Bisnovatyi-Kogan 2015) [5] and $M_{BH}(R_g)$ for a co-rotating orbit around an extreme Kerr hole ($\frac{a}{M_{BH}} = 1$). Accretion is more efficient for a rotating BH than for a stationary BH. However, the ISCO increases with $\frac{a}{M_{BH}}$ for counter-rotating orbit and approaches $9M_{BH}$ for an extreme Kerr BH [6] resulting in much lower efficiency.

A crucial parameter which governs accretion is the Eddington limit [7], equating the pressure gradient from the in-falling matter

$$\frac{dP}{dr} = \frac{-GM_{\odot}\rho}{r^2} \tag{2.28}$$

with the radiation pressure,

$$\frac{dP}{dr} = \frac{-\sigma_T \rho}{m_p c}\frac{L}{4\pi r^2} \tag{2.29}$$

we obtain the Eddington limit,

$$L_{Edd} = \frac{4\pi G M_{\odot} m_p c}{\sigma_T} \tag{2.30}$$

$$\simeq 10^{44}(\frac{M_{BH}}{10^6 M_{\odot}})erg.s^{-1} \tag{2.31}$$

where G represents the gravitational constant, c, is the speed of light, m_p the proton mass, σ_T the Thomson cross section. This is for accreting matter for TDEs with central engine mass, M_{BH}, scaled to $10^6 M_{\odot}$. The Eddington limit is regarded as an upper limit of the mass accretion rate. Note that the Eddington approximation assumes spherically symmetric accretion of a hydrogen gas. If $L \sim L_{Edd}$, the disk becomes geometrically thick. Geometrically thick accretion disk models determine the height of an accretion disk by a hydrostatic pressure equilibrium

$$\frac{1}{\rho}\frac{\partial P}{\partial z} = g_z^{grav}, \tag{2.32}$$

5. A Schwarzschild black hole (BH), is a BH with mass, but with no electric charge, and no spin. Karl Schwarzschild discovered this BH geometry at the close of 1915.

6. Kerr BH also referred to as spinning/rotating BHs possess mass and angular momentum without a charge. A BH with an electric charged is called the Kerr-Newman BH whereas if a BH has no angular momentum but has an electric charge its called the Kerr-Newman.

7. The Eddington limit approximates the maximum accretion rate by equating the radiation pressure and the accreting material.

where ρ and P represents the density of matter and the pressure within the accretion disk, respectively. The z-component of the gravitational attraction can be expressed as

$$g_z^{grav} = \frac{z}{(r^2 + z^2)^{\frac{3}{2}}} \tag{2.33}$$

$$\approx \frac{z}{r^3}, \tag{2.34}$$

whereas the radial component is balanced by the centrifugal force. When the accretion rates exceed a critical value, the accretion around the SMBH becomes optically thick (Paczynsky and Wiita 1980). A thick accretion disk forms when the accretion rate becomes large, reaching luminosities significantly above the Eddington limit. This behaviour is caused by a geometric effect such as the formation of cusps in the inner jet, which depends on the angular momentum distribution. Such large luminosities produce large radiation fields in the cusp region leading to the formation of collimated beams of relativistic particle outflow perpendicular to the accretion disk, i.e. the jet. The energy which is liberated during the accretion process is thought to be transferred outward by the same processes which take away the excess angular momentum. Some energy goes into driving coherent motions such as circulations or outflows (Blandford and Znajek 1977). The majority of the energy might also be dissipated as heat or radiation. Retention of this energy by the accretion flow will consequently lead to the associated pressure partially supporting the flow against gravity. This reduces the relative importance of rotation. When the local rotation rate is still a large fraction of the Keplerian value, the flow will resemble a disk-like accretion flow, but the added pressure force can cause mass loss (Blandford and Begelman 1999). A dominance in pressure support over rotational support, or even pressure support comparable to the rotational support, will result in the flow being inflated into a nearly spherical configuration and complex instabilities may arise.

As the stellar material makes its way back to the SMBH, vertical and horizontal compression occurs. This compression generates a shock that heats the gas and dissipates the kinetic energy (Rees 1988, Evans and Kochanek 1989). This accretion in a TDE system occurs within the super-Eddington regime.The receding debris and the incoming debris interact, resulting in the depletion of the kinetic energy of the debris at the expense of viscous heating (Piran, Sądowski, and Tchekhovskoy 2015). This causes the bound debris from the TDE to dissipate the ordered kinetic energy resulting in material moving closer to the SMBH. Efficient energy loss instigates material to be rapidly funnelled onto the SMBH, inducing a large amount of radiation in the process. Inevitably the bound portion of the debris stream gives rise to an acute period of accretion onto the SMBH. Furthermore, as material from the debris stream returns to the pericentre of the original star, an accretion disk is formed around the SMBH. A common assumption is that the TDE disk is in the plane of the SMBH's equatorial plane. An expanding disk contributes to the matter which is re-accreted at rates which may exceed the stellar fallback rates, although a disk wind may suppress this contribution to the central BH accretion rate. Viscous dissipation heats the gas while also transporting angular momentum through the system. This heat results in radiation flares. The accretion disk grows until a steady state. The matter in the accretion disk drifts gradually inwards until it reaches the ISCO of the BH, at this point the matter spirals into the BH.

A TDE disk that is misaligned with the spinning SMBH's equatorial plane would

precess around the SMBH's spin axis due to the Lense-Thirring effects (Stone and Loeb 2012, Kelley, Tchekhovskoy, and Narayan 2014). This would cause the jet axis to vary with respect to the observer's line of sight, resulting in variations in the hard X-ray light curve. Including torque effects to the disks has shown that typical TDE disk cannot complete one full precession period before aligning with the SMBH's equatorial plane (Ivanov, Polnarev, and Saha 2005). An observable consequence of the disk expansion is a change in the decay rate of the central accretion. This due to angular momentum storage. The disk will be driven into precession from Lense-Thirring torques, consequently aligning with the SMBH's spin over longer timescales. The spectrum of Swift J1644+57 (Bloom et al. 2011, Burrows et al. 2011, Levan et al. 2011,Zauderer et al. 2011) is highly non-thermal thus suggesting the presence of a jet contributing to the TDE flares. Precession could be a plausible explanation of the evolving quasi-periodic modulation of the Swift J1644+57 light-curve (Strubbe and Quataert 2011, Lei, Zhang, and Gao 2012).

The accretion rate during the initial phase of the TDE can proceed with a super-Eddington rate (Rees 1988). The large discrepancy between L_X and L_{Edd} may indicate beaming in the order of, $\Gamma \sim 10$. This beaming is a result of the jet formation. The jet emission is non-thermal with the accretion disk accounting for the thermal emission. In the late phase of TDE, new stellar matter continues to fall back at a diminishing rate $\dot{M} \propto t^{-\frac{5}{3}}$. The super-Eddington luminosity of Swift J1644+57 together with the variability in the light curve suggests that, most likely, X-ray photons are directly emitted from a beamed jet, moving at relativistic speed and pointing towards the observer (Burrows et al. 2011).

Jetted TDEs produce beamed X-ray emissions which are thought to originate from internal shocks at the base of the jet where shells of accelerated plasma can move at different velocities (Wang et al. 2011). It has been posited that the disruption of a star results in a thick envelope of $r_{out} \sim 3 \times 10^{15}$ cm around the SMBHs (Loeb and Ulmer 1997). The emitting region of the TDE is inside this circumnuclear envelope. This envelope material may have a wind density distribution $\rho_{env} \propto r^{-3}$,

$$\rho_{env}(r) = \frac{f_{TDE} M_*}{4\pi ln(\frac{r_{out}}{r_{in}}) r^3} \equiv \rho_{in} r_{in}^3 r^{-3} \tag{2.35}$$

where f_{TDE} is the fraction of the mass in the envelope which is the mass of the stellar debris that is bound to the SMBH whereas r_{out} and r_{in} represent the outer and inner radii of the envelope respectively. The non-thermal emission, which is produced due to the disruption, will only be visible if the jet breaks out.

While the jet is propagating inside the envelope with a sub-relativistic velocity, some energy is dissipated into the cocoon surrounding the advancing jet. As the jet advances into the ambient envelope, a bow shock forms at the head the jet. Particles may be accelerated within these shocks producing radio synchrotron radiation. High-energy neutrinos could be produced as well (Wang and Liu 2016). The tip of the jet consists of a termination shock and a reverse shock propagates back into the jet, where the jet is decelerated and heated.

Senno, Murase, and Mészáros 2017, calculated that powerful jets with $L \geq 10^{44}$ erg·s^{-1} can break out of the envelope successfully while jets with luminosity $L \leq 10^{44}$ erg·s^{-1} would be choked in the envelope (non-jetted TDE). In the non-jetted

TDE case, all the jet energy is transferred to the cocoon. TDEs with relativistic jets of $L > 10^{48}$ erg·s^{-1} imply that the accretion rates are $> 10^4$ higher than the Eddington accretion rate for a $10^6 M_\odot$ BH. As the jet breaks through the optically thick envelope the cocoon becomes optically thin.

2.4.5 Particle acceleration within the jets

In this section we will discuss how particles gain energy in astrophysical sources. For more details please refer to Rybicki and Lightman 2008, Böttcher, Harris, and Krawczynski 2012 and Grupe, Thomas, and Leighly 1999.

In 1949 Fermi proposed a mechanism in which particles can be accelerated in stochastic collisions. This process can be seen as the scattering of a particle by magnetic field irregularities (magnetic mirrors) in an interstellar cloud. Particles are assumed to be accelerated into a non-thermal energy distribution in astrophysical shock waves through this mechanism.

In this Section, we discuss the Fermi acceleration mechanism in the context of collisionless shocks, i.e. the shocks have energy and momentum transfer between particles mediated only by plasma processes. Coulomb scattering is negligible for the relevant astrophysical timescales. Furthermore the particle energies needed for Fermi acceleration to takes place exceed the thermal energies in the astrophysical environments. There are two kinds of Fermi acceleration: (i) first-order Fermi acceleration which commonly take place in shock waves (ii) second-order Fermi acceleration induced by moving magnetised gas clouds in astrophysical environments.
Suppose that a charged particle with energy E_1 (velocity, v) in the observer's frame is scattering against a moving boundary between regions of different density. The cloud (Figure (2.8)) acts as a massive scattering centre as a result of the inhomogenous magnetic fields generated by the charged particles.

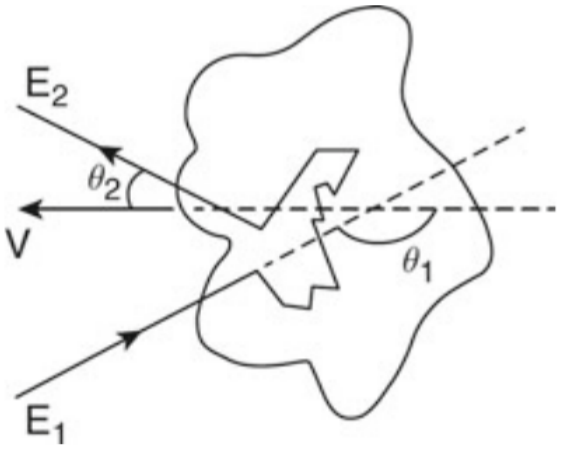

FIGURE 2.8: Scattering of a particle by a magnetized moving gas cloud. Credit:Gaisser, Engel, and Resconi 2016

Assume that the cloud has velocity $\beta_{cl} = \frac{v_{cl}}{c}$ and let θ_1 be the angle between the cloud velocity and the initial particle momentum, θ_2 is the angle between the cloud velocity and the final particle momentum. Define $\gamma_{cl} = \frac{1}{\sqrt{1-\beta_{cl}^2}}$ as the Lorentz factor of the cloud in the laboratory frame.

Additionally we assume that the particles are ultra-relativistic i.e. $E \simeq pc$ where p is the particle momentum and c is the speed of light. The energy of the particle E_1' in the cloud reference frame is given by

$$E_1' \simeq \gamma_{cl} E_1 (1 - \beta_{cl} cos\theta_1) \tag{2.36}$$

The cloud mass, M_{cl}, is much larger than the particle's mass, m, ($M_{cl} \ll m$). We assume that the particle is reflected inside the cloud i.e. no energy is lost or gained in the cloud's reference frame, hence $E'_1 = E'_2$ and in the laboratory frame the energy of the particle after the collision is :

$$E_2 \simeq \gamma_{cl} E'_2 (1 + \beta_{cl} cos\theta'_2) \tag{2.37}$$
$$= \gamma_{cl}^2 E_1 (1 - \beta_{cl} cos\theta_1)(1 + \beta_{cl} cos\theta'_2) \tag{2.38}$$

The relative energy change is given by

$$\frac{\Delta E}{E} = \frac{1 - \beta_{cl} cos\theta_1 + \beta_{cl} cos\theta'_2 - \beta_{cl}^2 cos\theta_1 cos\theta'_2}{1 - \beta^2} - 1 \tag{2.39}$$

The mean fractional energy gained by the particle is obtained by averaging $< cos\theta_1 >$ and $< cos\theta'_2 >$. The collision is the result of a large number of individual scatterings suffered by the particle inside the cloud. The particle gains energy when it exits the cloud opposite to its incoming direction ($\theta_1 = \pi$). The particle trajectory inside the cloud is isotropic because of the multiple scattering process, the exiting angle θ_2 is random

$$\langle cos'\theta_2 \rangle = 0 \tag{2.40}$$

The probability of a collision to occur between a particle and the cloud is not constant as a function of the relative angle θ_1. Conversely, the probability is proportional to the relative velocities of the cloud and particle, i.e. it is more likely for a particle to interact with an oncoming cloud than a cloud that is moving away from the particle.

Hence,

$$\langle cos\theta_1 \rangle \simeq \frac{\int_{-1}^{1} cos\theta_1 (1 - \beta_{cl} cos\theta_1) dcos\theta_1}{\int_{-1}^{1} (1 - \beta_{cl} cos\theta_1) dcos\theta_1} \tag{2.41}$$
$$= -\frac{\beta_{cl}}{3} \tag{2.42}$$

The energy after collision increases on average by a factor

$$\langle \frac{\Delta E}{E} \rangle \simeq \frac{1 - \beta_{cl} \langle cos\theta_1 \rangle}{1 - \beta_{cl}^2} - 1 \tag{2.43}$$
$$\simeq \frac{1 + \frac{\beta_{cl}^2}{3}}{1 - \beta_{cl}^2} - 1 \tag{2.44}$$
$$\simeq \frac{4}{3} \beta_{cl}^2 \tag{2.45}$$

This mechanism is known as the second-order Fermi acceleration mechanism which refers to the amount of energy gained during the motion of a charged particle in the presence of an inhomogeneous magnetic field. The second-order Fermi acceleration mechanism is stochastic and the energy gain can vary depending on the geometry of the scattering.

Shock waves are typically occur in regions consisting of moving magnetic field inhomogenities. As a particle travels from upstream to downstream through a shock wave, a magnetic field will be encountered. Hence the particle will be reflected back

upstream at an increased velocity. In light of the same process occurring the particle will gain additional energy. Bell 1978 and Blandford and Ostriker 1978 independently showed that Fermi acceleration by supernova remnant shocks is particularly efficient because the motions are not random. A charged particle in front of the shock front can pass through the shock and then be scattered by magnetic inhomogeneities behind the shock

Suppose θ_1 is the angle between the direction of the shock and direction of the incident particle, with the same convention as in Figure (2.8) this will lead to the magnetic mirror being constrained to a specific geometry : $-1 \leq cos\theta_1 \leq 0$. The probability of a particle hitting the shock with $cos\theta_1$ is proportional to $2\,cos\theta_1$, leading to equation (2.39) becoming

$$\frac{\Delta E}{E} \simeq -2\beta_{cl} cos\theta, \tag{2.46}$$

The probability of crossing the wave front is proportional to $-cos\theta$ thus equation (2.42) becomes

$$\langle cos\theta_1 \rangle \simeq \frac{\int_{-1}^{0} -cos^2\theta dcos\theta}{\int_{-1}^{0} -cos\theta dcos\theta} \tag{2.47}$$

$$= -\frac{2}{3} \tag{2.48}$$

The average energy gain for each particle is:

$$\langle \frac{\Delta E}{E} \rangle \simeq -2\beta_{cl} \langle cos\theta \rangle \tag{2.49}$$

$$\simeq \frac{4}{3}\beta_{cl} \tag{2.50}$$

The first-order comes from the fact that the energy gained per shock crossing is proportional to β_{cl}.

Chapter 3

Model set-up

The purpose of this Section is to discuss the model set-up of the hadronic code developed by (Böttcher et al. 2013). The TDE emission region is assumed to be described as a magnetized spherical blob of radius, R_{blob}. This region is injected with a non-thermal electron and proton distribution. The bulk Lorentz factor of the entire emission region is represented by, Γ, with a corresponding viewing angle, $\theta \sim \frac{1}{\Gamma}$. This model is referred to as the one-zone model for emission. Instabilities and shocks in this sphere are thought to accelerate particles to ultrarelativistic energies. These particles then radiate photons whose flux is amplified along the jet axis with a Doppler factor, δ. The particles radiate through various physical processes. The highly Doppler-boosted non-thermal electromagnetic emission is characterized by a Spectral Energy Distribution (SED) (see Figure (4.1))

High energy electrons lose their energy predominantly by synchrotron radiation and inverse Compton scattering (IC) whereas high energy protons lose their energy through synchrotron radiation, photopair (Beth-Heitler), and photopion production. Photopion production produces many unstable particles, such as pions ($\pi^{\pm}, \pi^{0}$), muons ($\mu^{\pm}$) and kaons ($K^{\pm}, K^{0}$), which then decay into lighter particles (equation (2.2)) . The charged pions and muons are assumed not to radiate because their decay timescales are much shorter than their synchrotron cooling timescale for all the relevant parameters in the model.

Mücke et al. (2000) showed that the most accurate and reliable evaluation of the radiative output from photo-pair and photopion production is best achieved through Monte-Carlo simulations. Monte-Carlo simulations refer to a statistical technique used to model probabilistic systems, such as particle scattering and also to establish the odds for different outcomes occurring. These tend to be time-consuming and computationally expensive, especially in the case of hadronic models. This is due to the complicated energy dependency of the $p\gamma-$ interaction cross sections involved in the process. This may be resolved through analytical expressions for the final decay products ($e^{\pm}$, photons, ν) from photo-pion production for isotropically distributed, mono-energetic photons and protons which have been developed by Kelner and Aharonian ((2008)). These functions require prior knowledge of the target photon field and the proton spectrum. Evaluating the effects of the cascades is preceded by the evaluation of the first-generation products. Ultra-high energy regimes are highly opaque to $\gamma\gamma$ productions; this also happens to be the energy range at which most of the electrons/positrons and π^{0} decay $\gamma-$ rays are produced.

The Kelner and Aharonian, (2008) templates neglect the synchrotron and Compton emission from intermediate decay products such as muons and pions. These

emissions may contribute to the high-energy spectra (Mücke et al. 2003). One may neglect these contributions if one of the following conditions are met:

1. The synchrotron cooling timescale of the intermediate decay products has to be longer than their decay timescales.

2. Proton synchrotron losses have to strongly dominate over the photo-pion interactions while neglecting external radiation fields as target field for particle and photon interaction and cascading.

We note that due to these caveats, the hadronic model does not favour situations with both large magnetic field strengths and a large emission region. In such a case the photo-pion production would dominate over the proton synchrotron emission, and the synchrotron cooling timescales of the intermediate decay products must be shorter than their decay scales (see Böttcher et al. 2013).

The steady-state hadronic transfer code neglects pion and muon synchrotron radiation. This restricts the maximum possible field strength as a function of the maximum proton energy injected into the emission region. Protons may lose their energy radiatively via the proton synchrotron losses or photomeson productions.

The radiative output in the model is kept consistent with the observed SED of Swift J1644+57 while varying the magnetic field strengths and blob radii. The input parameters of the radiative code are related to the characteristics of the source, such as the black hole mass $M_{BH} = 2 \times 10^6 M_\odot$ (Hayasaki, Stone, and Loeb 2016 and Levan et al. 2016) and redshift of $z = 0.345$ (Burrows et al. 2011). The emission region moves along the jet with bulk Lorentz factor, $\Gamma = 10$ (Burrows et al. 2011), at a viewing angle, $\theta = 5.73°$. The model is constrained by observed data points in the optical, X-ray and the TeV and GeV energy ranges by the VERITAS and Fermi limits, respectively. We set the electron and proton injection as a power-law with spectral index $q_e = 2.2$ and $q_p = 2.6$, respectively. The fits require low electron injection energies, $\gamma_{min} = 10$ and $\gamma_{max} = 200$ to produce satisfactory fits for the optical- X-ray data.

The Schwarzschild radius of a SMBH, $R_s = 3 \times 10^{11} \frac{M_{BH}}{10^6 M_\odot}$ cm, gives a lower limit to the size of the emission region. It is generally expected that the emission region should be an order of magnitude larger than R_s, thus we only consider values larger than R_s. Subsequently, the maximum emission region size is assumed to be limited by comparing the light-crossing $\frac{R}{c}$ time to the observed variability timescale. The variability time scale, $\Delta t_{var}^{obs} \sim 10^6 s$, constrains the size of the emission region, $R \leq \frac{c \Delta t_{var}^{obs} \delta}{1+z} \lesssim 2 \times 10^{17}$ cm . Based on the variability time scale, one can estimate the distance of the emission region from the black hole at $\sim 4 \times 10^{16} \Gamma^2 \Delta t_{10^6 s}$ cm. The injection luminosity and proton kinetic luminosity are adjusted until a reasonable fit is obtained, while varying the magnetic field and blob radius.

3.1 Radiation processes

The flux density of photons and neutrinos is measured as the energy flux in erg per unit area per unit time per unit frequency or unit energy for neutrinos.The flux density is typically fitted to a power-law over a small frequency range (see Figure(4.3)). Astrophysical jets such as Blazars typically have strong continuum emission extending from the radio all the way to the $\gamma-$ray regimes. This is represented as a Spectral Energy Distribution (SED). An SED shows the photon frequency ν times the differential energy flux F_ν as a function of the log ν. The SEDs displays which part of the spectrum carries most of the energy emitted by the jet. The energy flux per linear frequency interval is given as $F_\nu = \frac{dF}{d\nu}$ and the energy flux per logrithmic frequency interval $\nu F_\nu = \frac{dF}{dlnv}$. Plotting νF_ν , usually expressed in units of $erg \cdot cm^{-2} \cdot s^{-1}$, vs log ν leads to the area below the curve being proportional to the energy emitted by photons in a certain log ν interval.

High energy photons can be produced by radiative processes, in particular, those involved in the interaction of VHE charged particles (leptons and hadrons) with targets such as radiation fields and magnetic fields. The text from this section has been inspired by Grupen et al. 2005, Mannheim 1993 and Ghisellini 2013.

3.1.1 Electron Synchrotron

Consider a particle with mass, m , electric charge, q, and energy per particle, $E = \gamma mc^2$, and speed, βc. Assuming that this particle is moving in a magnetized region, with magnetic field strength, B, it will follow a spiral trajectory. The deflection of a particle in a magnetic field gives rise to accelerated motion. According to classical electrodynamics this accelerated motion will lead to radiation (see Figure (3.1)). If the particles are non-relativistic or relativistic, the radiation is called cyclotron and synchrotron radiation, respectively.

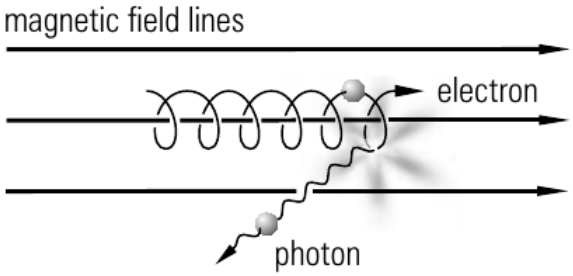

FIGURE 3.1: Synchrotron emission due to a deflected particle in a magnetic field. credit : Grupen et al. 2005

In the presence of no electric field the only acting force is the relativistic Lorentz force;

$$F_L = m\gamma\dot{\bar{v}} = \frac{q}{c}(\bar{v} \times \bar{B}), \tag{3.1}$$

in the magnetic field, where $\gamma = (1 - \frac{v^2}{c^2})^{-\frac{1}{2}}$ is the Lorentz factor and v is the velocity of the charged particles. The parallel and perpendicular Lorentz force components are;

$$F_{L\parallel} = \gamma m\frac{dv_\parallel}{dt} = 0 \rightarrow a_\parallel = 0 \tag{3.2}$$

$$F_{L\perp} = \gamma m\frac{dv_\perp}{dt} = q\frac{v_\perp}{c}B \rightarrow a_\perp = \frac{qvBsin\theta}{\gamma mc} \tag{3.3}$$

We can also derive the Larmour radius r_L by assuming that $a_\perp = \frac{v_\perp^2}{r_L}$, which results to

$$r_L = \frac{v_\perp^2}{a_\perp} = \frac{\gamma m c^2 \beta sin\theta}{qB} \tag{3.4}$$

The characteristic frequency is the inverse of the time it takes to complete one orbit (gyration frequency), $\nu_g = \frac{c\beta sin\theta}{2\pi r_L}$, leading to

$$\nu_g = \frac{qB}{2\pi\gamma mc} = \frac{\nu_L}{\gamma} \tag{3.5}$$

where ν_L is the Larmor frequency, $\frac{qB}{2\pi mc}$, for sub-relativistic particles. Smaller magnetic fields lead to larger r_L, therefore smaller gyration frequencies. To establish and maintain an isotropic particle pitch-angle distribution, the pitch-angle scattering processes which cause particle isotropization should operate on a timescale shorter than the energy loss timescale [1]. The energy-loss of the particle in the magnetic field is,

$$(\frac{dE}{dt})_{sy}(\theta) = -\frac{16\pi c}{3}(\frac{q^2}{mc^2})^2 u_B \beta^2 \gamma^2 sin^2\theta \tag{3.6}$$

where $u_B = \frac{B^2}{8\pi}$ is the energy density in the magnetic field. The electron synchrotron energy-loss, expressed in terms of the rate of change of the electron Lorentz factor ($\frac{dE}{dt} = m_e c^2 \frac{d\gamma}{dt}$), averaged over all pitch-angles,

$$-(\frac{d\gamma}{dt})_{syn} = -\dot{\gamma}_{sy} = \frac{4}{3} c \sigma_T \frac{u_B}{m_e c^2} Z^4 (\frac{m_e}{m})^3 \beta^2 \gamma^2 \tag{3.7}$$

$$\xrightarrow[\gamma \gg 1]{} \frac{4}{3} \sigma_T c \gamma^2 \frac{u_B}{m_e c^2} \tag{3.8}$$

where Z is the particle's charge in units of the elementary charge, e.

In Equation (3.6) and (3.8) we notice that the synchrotron energy loss of relativistic particles scales with mass as $\frac{dE}{dt} \propto -m^{-2}$ and $\frac{d\gamma}{dt} \propto -m^{-3}$. Hence, for a proton to undergo the same energy loss $\frac{dE}{dt}$ as an electron with Lorentz factor, γ_e, the proton would have to have a Lorentz factor of $(1836)^2\gamma_e$, for this reason electrons are the most efficient radiators (Böttcher, Harris, and Krawczynski 2012).

3.1.2 Proton Synchrotron

Consider a proton with the same energy as an electron $E_e = E = E_p$. The Larmor frequency of the proton can be rescaled by $\frac{m_p}{m_e} \simeq 1836$. The energy loss rate of protons $(\frac{dE}{dt})_{sy}$ is a rescaled by a factor $(\frac{m_p}{m_e})^2 \simeq 10^6$ times slower than the energy loss rate of electrons. The characteristic frequency of the synchrotron radiation $\nu_c = \frac{3}{2}\nu_L(\frac{E}{mc^2})^2$ emitted by a proton is a factor $(\frac{m_p}{m_e})^3 \simeq 10^9$ times smaller than that of an electron with the same energy. The synchrotron cooling time of a proton is

$$t_{sy} = \frac{6\pi m_p^4 c^3}{\sigma_T m_e^2 E B^2} \tag{3.9}$$

1. The time needed for converting the particle energy into radiation

The efficiency at which a particle can lose energy through synchrotron losses is $\frac{t_{var}}{E}\frac{dE}{dt}_{syn}$ in the coming-frame. Combining the requirement that the efficiency must be larger than one such that the efficient dissipation of energy via synchrotron radiation is met, with the Hillas condition [2]

$$E = qBR, \tag{3.10}$$

will give a range of allowed energies at which efficient synchrotron radiation will be possible. This is contingent on the magnetic field strength in the blob.

Proton synchrotron radiation is a hadronic mechanism that could be important in TDEs but requires highly magnetized jets. Highly magnetized jets require that the electron energy distribution peak at lower energies. Low electron energy densities in the emitting region make it harder to scatter SSC (Synchrotron-Self Compton) radiation to TeV energies (see Figure (4.1)), therefore requiring that a larger fraction of the flux of the SED should have a hadronic origin.

A smaller emission regions makes the blob more opaque to $\gamma\gamma \rightarrow e^+ + e^-$ attenuation.This makes it difficult to explain the luminous VHE/TeV radiation from astrophysical sources with a proton synchrotron model.

3.1.3 Electromagnetic cascades in jets.

In VHE astrophysical sources, a range of cascades can form depending on the target matter, radiation, the compactness, and magnetic field strength in this region. Electromagnetic Compton synchrotron cascade induced by energetic electrons can be produced by making $\gamma-$rays in a region that is optically thick to $\gamma\gamma-$pair production attenuation. On the other hand, ultra-relativistic protons interacting with an ambient target photon field and matter will form secondaries that can initiate an electromagnetic cascade. Photons produced by $\pi^{\pm}$ ('$\pi^{\pm}$' cascade) and π^0 ('π^0 cascade') decay and the synchrotron emissions from $e^{\pm}$ produced from the $\pi^{\pm}$ channel can reach energies of up to $m_e c^2 \gamma_{p,max}$.

Neutrinos produced in the emission region escape directly whereas photons, electrons and positrons form an electromagnetic cascade. Synchrotron radiation and Compton scattering are the dominant electromagnetic processes. High energy $\gamma-$rays can escape from the source if the optical depth, τ, to produce $e^{\pm}$ pairs with ambient soft photons is less than unity, $\tau < 1$.

The leptonic part of our code contains the low-energy electrons making the low-frequency synchrotron emission component. The first generation of the cascades is obtained from the pion decay. The injection rate, stationary state of pair distribution as well as the associated synchrotron emission are also computed. The synchrotron photons from pairs are still energetic enough to produce a second generation of pairs cascade, which can also produce a third generation, and so on. We then iterate the process until the pairs give a negligible contribution with respect to the sum of the

2. If a particle escapes from its place of acceleration, it will not be able to gain more energy. Requiring that the Larmour radius of a particle may not exceed the size of the acceleration region places a geometric criterion referred to as the Hillas criterion/ Hillas condition.

previous generations. During the computation of the cascade spectrum, the low energy photon field is considered as being represented only by the synchrotron emission of primary electrons, neglecting the emission from the cascade itself, i.e. assuming that the cascade is not self-supported.

The maximum proton energy depends on the most rapid cooling mechanism (see Figure (4.2)). If primary particles lose energy in an interaction, e.g. protons in pion photo-production $p + \gamma \rightarrow p + \pi^0$, this process can be interpreted as cooling, whereas if the primaries disappear, such as protons in $p + \gamma \rightarrow n + \pi^+$ it is interpreted as an escape. Protons in hadronic models are typically assumed to be accelerated in the relativistic outflow together with electrons and positrons by processes such as Fermi shock acceleration. This acceleration can happen at shock fronts, moving through the jet. At these shock fronts, these particles are accelerated by the first-order Fermi mechanism. The first-order Fermi acceleration mechanism injects electrons and protons with a power-law distribution between electron Lorentz factors $\gamma_{min} \leq \gamma \leq \gamma_{max}$ for the downstream of the shock front. The particles gain a constant fraction of energy by passing through the shock front. This transition is repeated many times to achieve high energies. The accelerated protons can now interact with radiation fields within the jet. The rate of acceleration of the protons to an energy, E, $t_{acc}^{-1} = E^{-1}\frac{dE}{dt}$ is given by

$$t_{acc} \sim \eta \frac{E_p}{eBc} \tag{3.11}$$

$$= 1.1 \times 10^2 \eta E_{15} B^{-1} s, \tag{3.12}$$

where η is the acceleration efficiency and B is the magnetic field strength which is needed to accelerate protons to large energies, $E_{15} = \frac{E}{10^{15}} eV$. Charged particles of mass, m, and energy, $E = \gamma mc^2$ will emit synchrotron radiation at a rate $t_{sy} \simeq 5 \times 10^{11} E_{15}^{-1} B^{-2} s$. Comparing these two quantities, we can derive $E_{p,cut-off} \simeq 6.7 \times 10^{19} B_G^{\frac{-1}{2}} eV$, which is the energy cut-off of the proton spectrum. This has a corresponding cooling timescale $t_{acc} = t_{sy}(E_{max}) \simeq 7.4 \times 10^6 B_G^{\frac{1}{2}} s$.

3.2 Expected neutrino detection probability

The flux per energy of the neutrino spectra is represented as

$$F_\nu = E_\nu \phi_\nu \tag{3.13}$$

F_ν is the all-flavour neutrino flux. The neutrino flux density is given as

$$\phi(\nu, E_\nu) = \frac{dN_\nu}{dE_\nu \Delta t dA} \tag{3.14}$$

where N_ν is the particle number, dE_ν is the energy range, Δt is the duration of the TDE flare whereas dA is the differential area on which the flux is impinging (see Figure (3.2)). The sample (IceCube IC86) is composed of three years of data taken with the 86-string configuration from 15^{th} May 2012 till 18^{th} May 2015.

The relation between the neutrino flux from a point source and the rate of events in a detector, $\dot{N}_\nu$, can be written as:

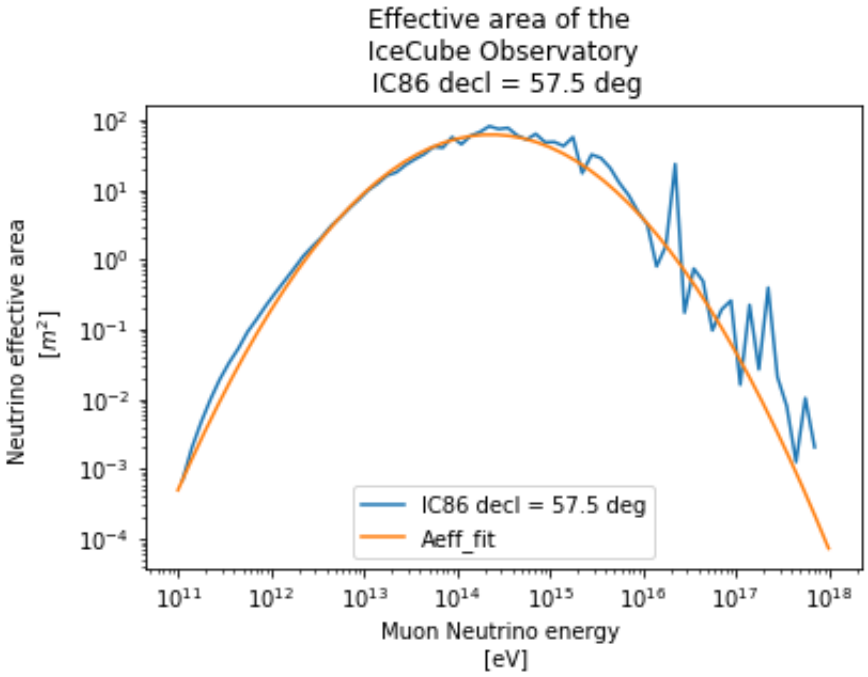

FIGURE 3.2: The effective area as a function of energy in IceCube IC86 configuration. Swift J1644+57 has declination +57 34 59.7 motivating the choice of the declination. This effective area is given by the data set IC86-2011 (solid blue line) while the orange line is a fit of the blue line using MINUIT. F. Oikonomou priv. communication (also see Oikonomou et al. 2019 Section 3.4).

$$\dot{N}_v = \int \phi(v, E_v) A_{eff} dE_v \tag{3.15}$$

$\phi(v, E_v)$ is the differential flux for neutrinos in the detector, $A_{eff}(\theta, E_\nu)$ represents the zenith and energy-dependent IceCube effective area for a neutrino arriving with zenith angle θ and energy, E_ν. The effective area mimics the area of a perfect detector i.e. a detector configuration with a 100% detection efficiency which might produce the same event rate as the detector.

To obtain the number of neutrinos detected from a given TDE is given by;

$$N_\nu = \int_{E_i}^{E_f} A_{eff} \phi(\nu, E_\nu) \Delta t dE_\nu \tag{3.16}$$

where E_i and E_f represent the energy range ($10^{11} - 10^{18}$ eV) of the neutrinos, $\Delta t = 10^6$s is the duration of the TDE flare. The data sample used, in this study, to determine the effective area is the IC86. Figure (3.2) shows the effective area of IceCube-IC86 as a function of energy at the declination corresponding to our source.

We consider the effective area of IceCube out to $\sim 10^{18} eV$. We fit the IceCube effective area with a log parabolic function, $A * (4.3 * (\frac{E}{E_0})^{(0.3*(a-b*log(\frac{E}{E_0})))})$. We fix the reference energy $E_0 = 5 \times 10^{13}$ and therefore the spectrum is determined by the three unitless parameters A = 9 , a = 2 and b = 0.25. Figure (3.2) shows the effective

area of IceCube-IC86 as a function of energy at the declination 57.5° [3], which is close to the declination of Swift J1644+57

3. "NASA Telescopes Join Forces to Observe Unprecedented Explosion". Chandra Press Release: 7. 2011. Bibcode:2011cxo..pres....7. Retrieved 2011-04-21.

Chapter 4

Results and Evaluation of results

In this Section, we present the parameter study and discuss the implications of our results. We work under the assumption that the jets of the TDE produce high-energy emission primarily through relativistic protons. The proton distribution is described with a power law with an exponential cutoff function having proton spectral index $q_p = 2.6$. We performed numerous simulations using the radiative transfer code (Böttcher et al. 2013). Some of the results will be displayed and discussed below. All the model fits in this study require bulk kinetic jet powers in the relativistic protons in the range $L_p \sim 10^{47} - 10^{52} erg \cdot s^{-1}$. Luminosities as large as L_p in this study are only acceptable if the emission region if $R_{blob} > 10^{14}$cm (Crumley et al. 2019).

In this study if $R_{blob} < 10^{14}$ cm photo-pion emissions will dominate over proton synchtron emission and not produce a desired fit. Values smaller than this blob radius will violate the second limitation of the model (see Chapter (3)) and thus over predicting the TeV - GeV energy regime. The models produced acceptable SED fits, when we set $B = 60$ to 100 G as well as $R_{blob} = 10^{15}, 10^{16}$ and 10^{17} cm. The injection luminosity and kinetic luminosity are adjusted to maintain the same overall flux levels. The term "acceptable" fit refers to a model SED that passes through most observational points.

Parameters	Value
Injection luminosity [erg/s]:	1×10^{42}
γ_{min}:	10
γ_{max}:	200
Injection electron spectral index:	$q_e = 2.2$
Magnetic field at z_0 [G]:	60
Bulk Lorentz factor:	$\Gamma = 10$
Blob radius [cm]:	1×10^{15}
Black hole mass [$M_\odot$]:	2×10^6
Observing angle [degrees]	$\theta_{obs} = 5.73$
Redshift	Z = 0.345
Proton high-energy cut-off :	1×10^8
Proton spectral index :	$q_p = 2.6$
Kinetic luminosity in protons [erg/s]:	1×10^{53}

TABLE 4.1: Baseline model parameter values used for Hadronic Model Fit for Swift J1644+57 used to plot Figure (4.1)

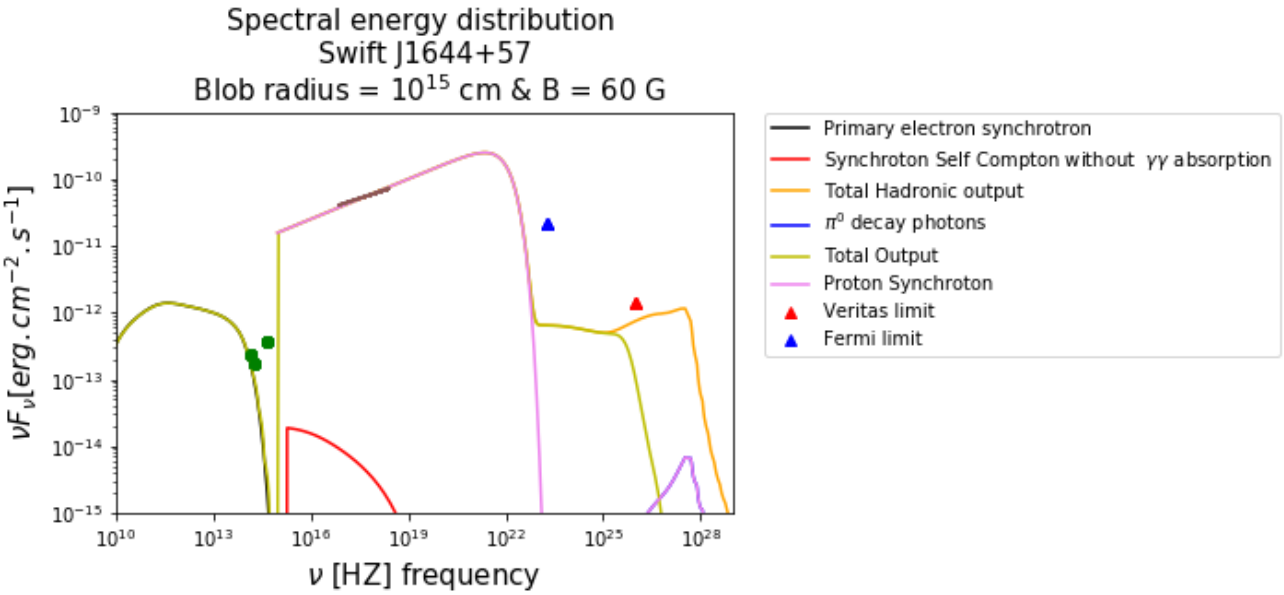

FIGURE 4.1: This SED was produced using the baseline parameters from Table (4.1). The total radiative output is constrained by optical and X- ray data points and by the VERITAS (red) and Fermi (blue) limits in the $\gamma-$ray regime. The black, red, brown, cyan, yellow and violet curves represent the primary electron synchrotron, SSC without $\gamma\gamma$ absorption, the total hadronic model and proton synchrotron emissions of the jet.

The Synchrotron-Self-Compton (SSC) [1] component is suppressed severely due to the large magnetic field and the relatively low energy electron synchrotron photons. The electron density, u_e, in the emission region is relatively low thus suppressing the IC emission which is negligible compared to the emission from the hadrons as well as the secondary particles coming from $p\gamma-$ interactions. The emission from electrons/positrons produced by the $\pi^{\pm}$ decay and from the photons coming from the π^0 decay contribute to the synchrotron-supported electromagnetic cascade.

The proton synchrotron component is promoted by large magnetic fields and a relatively high value of the maximum proton kinetic energy. The source must also possess a very high acceleration efficiency, $\eta_{acc} = 1$, under magnetically dense environments (see the timescale plots in Figure (4.2)). Large magnetic fields of the order $\sim$ 10 G are adopted in our model to overcome the slow cooling timescales of protons. Under these conditions, the protons can cool down with timescales $t_{sy} \sim 10^5$ s, shorter than the co-moving frame variability timescales $\Delta_{var}^{obs} \sim 10^6$ s. The large magnetic field requirement is typical for proton-synchtron models. This is also motivated by our choice of R and assuming a jet-opening angle $\frac{1}{\Gamma}$, the distance from the central core $\sim 4 \times 10^{16}\Gamma^2\Delta t_{10^6 s}$ cm, where $B \sim 100$ G can be expected (Barkov et al. 2012). The protons remain un-cooled before escaping i.e. t_{sy} and t_{esc} are competing processes having comparable values at the highest proton energies (see Figure (4.2)). At these high-B regimes the electrons are in the fast-cooling regime.

The observed X-ray spectral shape is fitted by proton synchrotron emission, such that the model does not over predict the $\gamma-$ray flux due to reprocessing of UHE $\gamma-$ray emission in cascades. The cut-off of the proton synchrotron emission represents the maximum proton energy (Aharonian 2000). This cut-off occurs when the synchrotron cooling and acceleration timescales are equal, equating the two timescales gives us the maximum energy at which protons can be accelerated to in the jet. In Figure (4.2) we notice that the maximum energy of the protons is $E_p^{max} \sim 10^{19}$ eV. In this parameter study, the code does not determine $\gamma_{p,max}$ self-consistently through the constraints that we have derived in Chapter (3), but we make sure that the maximum energy is below this $\gamma_{p,max}$. Protons will not be accelerated at energies where $t_{sy} < t_{acc}$ is met. The spectral fits required maximum energies for the protons of around $E_p \sim 10^{17} eV$ to reproduce the gamma-ray spectra. The proportion between the proton-synchrotron and high-energy photo-pion induced tail in Figure (4.1), shows that most of the protons radiate most their energy due to synchrotron loses.

The electron synchrotron and SSC is used as the target photon field for photo-pion production of the hadronic component and for evaluating the $\gamma\gamma$ opacity in the emission region. The protons interact with the target photon field to produce the synchrotron induced electromagnetic cascade. The acceleration timescale of the protons is inversely proportional to the magnetic field, $t_{acc} \propto B^{-1}$. At larger magnetic fields the acceleration timescale decreases, therefore protons may be accelerated to higher energies, but the synchrotron cooling timescale decreases as B^{-2}. This leads to proton synchrotron radiation becoming more dominant over photo-pion processes, where larger magnetic field strengths produce a smaller cascade component. The acceleration process continues until the rate at which the protons' loss rate

1. SSC process occurs when non-thermal electrons Compton scattered the synchrotron photons which they radiate. SSC is significant only when the electrons densities are relatively high.

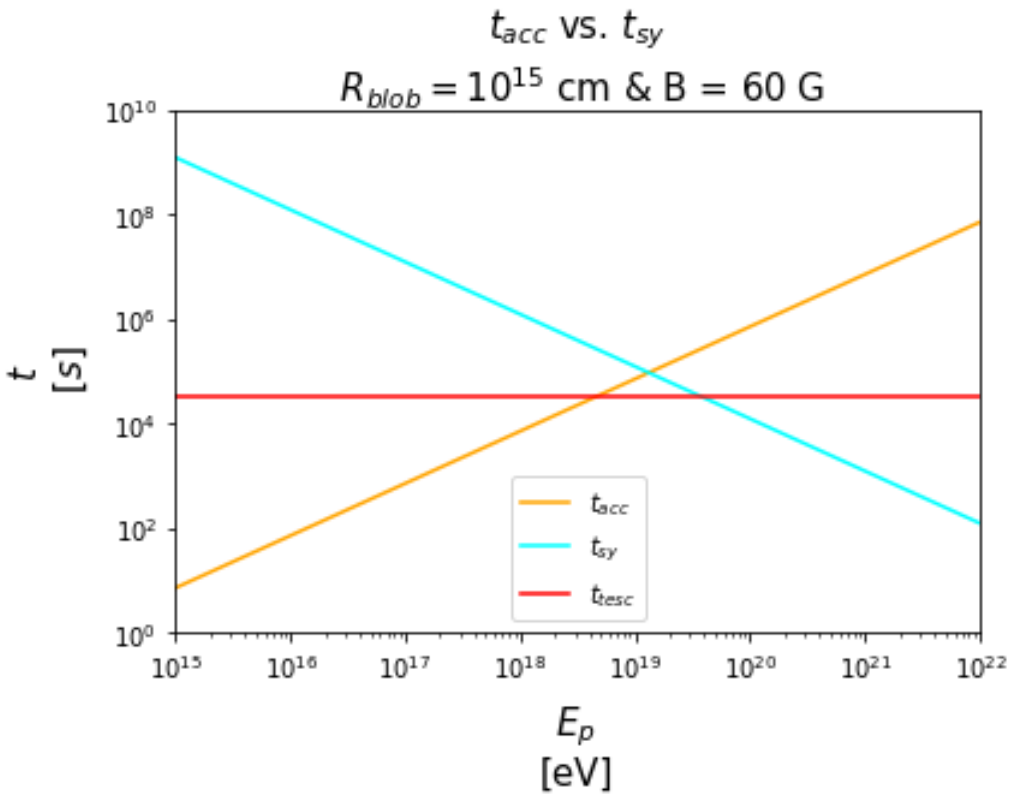

FIGURE 4.2: Acceleration and cooling timescales for the Swift J1644+57 SED described in Chapter (3). The red line represents the characteristic timescale of the emission region, the orange line represents the acceleration timescales whereas the cyan line represents the cooling timescales. The corresponding maximum value of the proton energy is $\sim 10^{19}$ eV.

is greater than the rate at which they gain energy.

The proton synchrotron radiation is the dominant emission for the second hump for all our SED fits for magnetic fields ranging from 60 to 100 G and blob radii $10^{15} - 10^{17} cm$. So, only a small fraction of the proton energy is available for the secondary particles. As a consequence, all the hadronic model fits have total jet power dominated by protons (see Figure (4.8)). Hadronic models such as Mücke et al. 2003 which consider charged π/μ synchrotron radiation could lower the strength of the electromagnetic component, thus decreasing the proton contribution in the jet power while increasing the magnetic field strength.

Neutrinos, unlike protons and electrons, escape the emission region without further interaction. We obtained the predicted neutrino spectrum for Swift J1644+57 is show by Figure (4.3) as explained in Section (3.2). We calculate the neutrino emission from the source itself, while excluding any additional contributions from escaping cosmic rays interacting, while propagating through the cosmic microwave background radiation. The resulting neutrino spectrum above $E_\nu \sim 10^{11}$ eV is $\frac{dN_\nu}{dE_\nu} \propto E_\nu^{-1.4}$ below this energy the neutrino spectrum is $\frac{dN_\nu}{dE_\nu} \propto E_\nu^{-1.4}$ because of the target photon field being steeper at that energy range. Neutrinos with energy 10^{14} eV are mostly

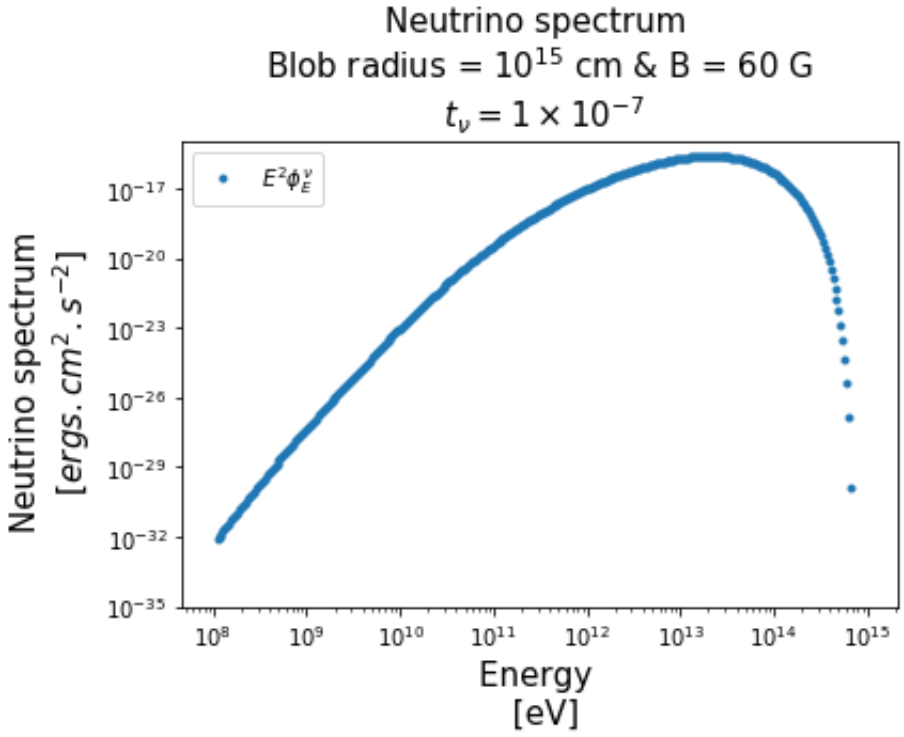

FIGURE 4.3: The all-flavour neutrino spectrum corresponding to the baseline parameters (Table 4.1, Figure (4.1)). This neutrino spectrum peaks at $\sim 10TeV$ and has a corresponding neutrino detection rate, $t_\nu = 1 \times 10^{-7}$.

produced near threshold in the Δ-resonance region, while the higher energy neutrinos are mainly produced in the secondary resonant region of the pion production cross-section.

Figure (4.4) shows the superimposed SED model fits with parameters $R_{blob} = 10^{15}$ cm and magnetic field varying from $B = 60$ to 100 G. The cascade component decreases in amplitude as the magnetic field increases. This is attributed to the fact that with an increase in the magnetic field, lower proton energies are required to produce the same proton synchrotron photons.

The neutrino spectra, from Figure (4.5), peak at $\sim 10TeV$ which falls within the observed IceCube neutrino range (1TeV - several PeV) (Aartsen et al. 2017). When the magnetic field strength was varied from 60 to 100 G and the blob radius $R_{blob} = 10^{15}$ cm was kept unchanged. The neutrino detection probabilities vary between 1×10^{-7} to 2×10^{-8}.

Figure (4.6) shows the superimposed SED model fits, keeping the magnetic field constant, 60 G, and varying the blob radius from 10^{15}, to 10^{16} and 10^{17} cm. In Figure (4.6) we notice that increasing the blob radius leads to an increase in the amplitude of an electron synchrotron component of the SED while the proton synchtron component remains. Increasing the blob radius leads to a decrease in the target photon density. The decrease in the target photon density leads to a reduction in the proton-photon interaction rate. The $\gamma\gamma$ opacity also decreases with an increase in blob radius, subsequently resulting in a decrease in the electromagnetic cascade

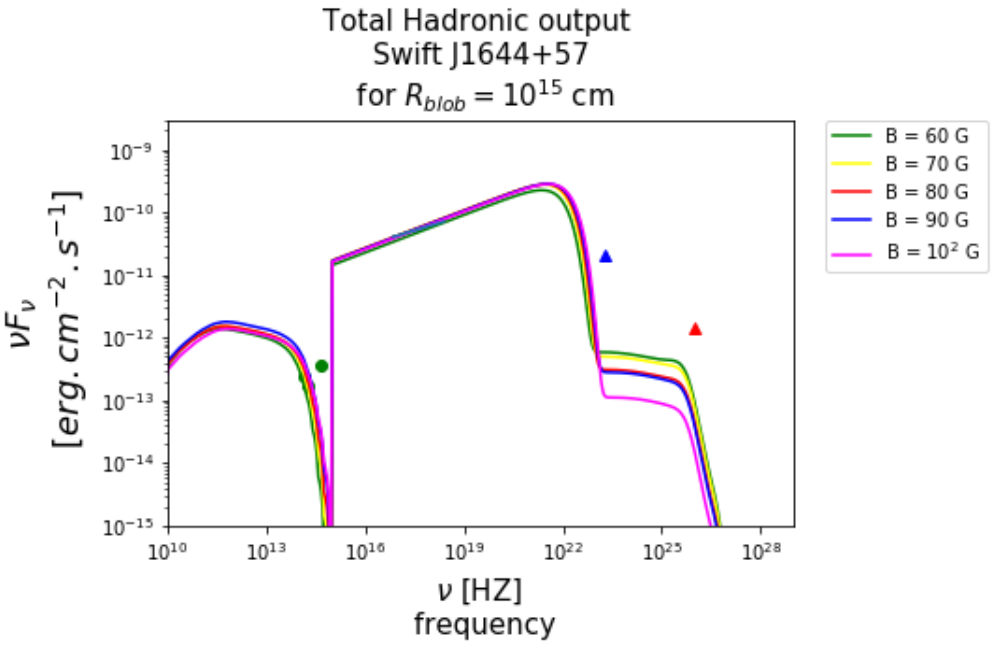

FIGURE 4.4: The SED multi-plot shows the result of varying 60 Gauss to 10^2 Gauss. The blob radius is kept constant at $R = 10^{15}$ cm while other parameters, such as the injection electron luminosity and the kinetic proton kinetic luminosity, were adjusted accordingly.

component. A change in R_{blob} did not have any significant impact on the proton synchrotron cut-off, because the magnetic field is kept constant.

Figure (4.7) shows the neutrino spectra corresponding to Figure (4.6). We noticed that in Figure (4.6) the fit with blob radius 10^{15} cm was the only spectrum which produced a pronounced cascade component. The target energy density has an anti-correlated relation to the blob radius. The electromagnetic cascades are suppressed with an increase in the blob radius thus decreasing the neutrino flux. The detection probabilities vary from 1×10^{-7} to 5×10^{-15}, which is in agreement with the previous statement. Seemingly varying the blob radius left the neutrino spectrum peak unchanged and all the spectra peak at $\sim 10TeV$.

The SED in Figure (4.1) would be produced by a TDE flare which carries kinetic power in relativistic protons $L_p \sim 1 \times 10^{53} erg \cdot s^{-1}$ as well as magnetic field luminosity $L_B \sim 1.35 \times 10^{45} erg \cdot s^{-1}$. This inequality of jet luminosities in protons and the magnetic field implies equipartition of energy does not hold in this case. It has been discussed in the literature (Sakurai 1987 ; Beskin, Kuznetsova, and Rafikov 1998) that electromagnetic energy can be converted into kinetic energy a few parsec from the central engine (Sikora et al. 2005). This happens at a point $\epsilon_{B,p} = \frac{L_B}{L_p} \sim \mu^{\frac{2}{3}}$, where $\epsilon_{B,p}$ is the magnetization factor and $\mu \equiv \frac{L_B + (\Gamma - 1)\dot{M}c^2}{\dot{M}c^2}$ being the total to rest-mass flux ratio. For relativistic jets $\mu \gg 1$. Unsteady, matter-dominated jets caused by internal shocks may lead to $\epsilon_{B,p} \ll 1$. This means that the magnetic-to-kinetic energy conversion should occur with a distance, $d_{flare} \sim (\frac{t_{flare}}{10^6 s})(\frac{\Gamma}{10})^2$ pc . In a case where the jet is proton dominate we have $\mu \simeq \frac{L_p}{\dot{M}c^2} \simeq \Gamma$ and find that the jet conversion occurs at a distance $d_{conv} \sim (\frac{d_c}{30 R_g})(\frac{M_{BH}}{10^6 M_\odot})$ pc (Sikora et al. 2005)

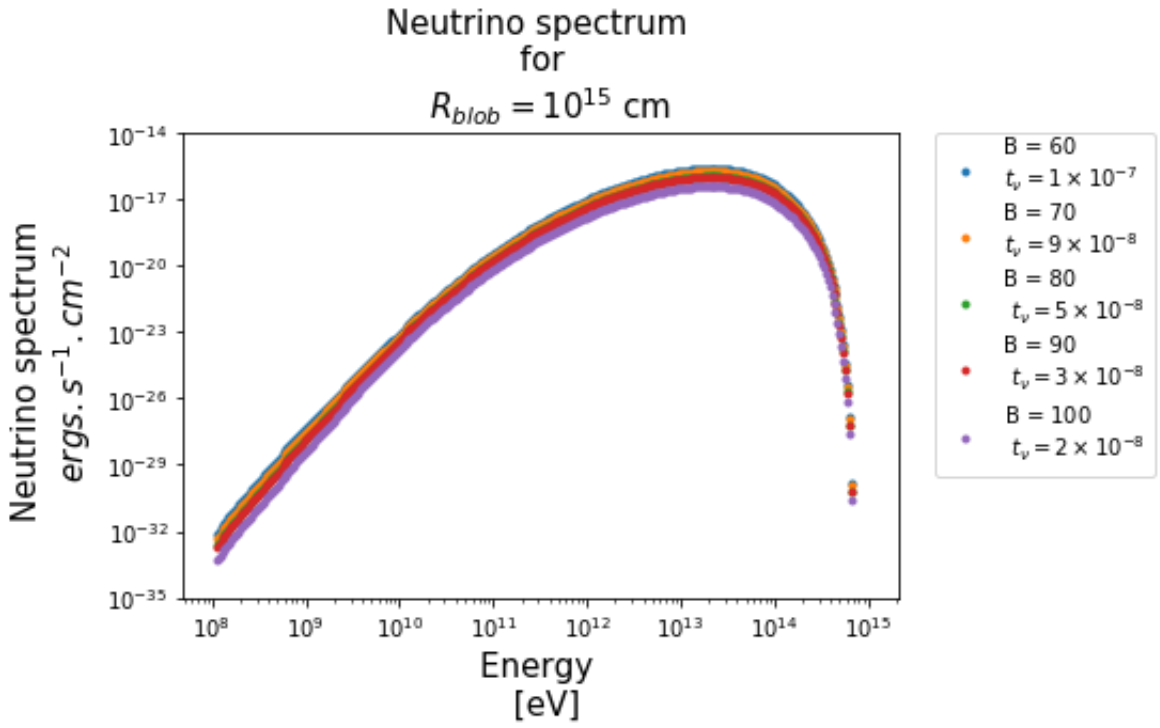

FIGURE 4.5: The superimposed all-flavour neutrino ($\nu + \bar{\nu}$) spectra with parameters corresponding to Figure (4.4) .

As long as the proton synchrotron cooling time and the escape time of the protons are of the same order of magnitude, the proton synchrotron model offers a significant efficiency of transformation of the kinetic energy of protons to hard synchrotron X-ray emission. The X-ray flux from Swift J 1644+57 varied on a time-scale $\delta t_{obs} \sim 10^2$ s, suggesting that the emission may have been produced at a distance of $2c\delta t_{obs}\Gamma^2 \sim 6 \times 10^{14}$ cm.

The presence of the electromagnetic cascade leads to the requirement of a disproportionately large proton luminosity as compared to the magnetic field luminosity. If $L_p \gg L_B$ this would imply that the dissipation may be due to internal shock dominance in the jet (Sikora et al. 2005). The variability in radio to optical bands in Blazars has been modelled by shocks moving along the jet axis (Hughes, Aller, and Aller 1989) which require particle dominance in the jet. These shocks would be responsible for particle acceleration. The fit in Figure (4.1) correspond to a magnetisation factor $\epsilon_{B,p} \sim 1.23 \times 10^{-8}$, thus suggesting that the jet is particle dominated. This implies that in an originally Poynting flux dominated outflow, the magnetic energy was efficiently converted into particle kinetic energy. This conversion may be due to dissipation caused by internal shocks (Sikora et al. 2005). This proves to be problematic for models arguing that electromagnetic energy is extracted from the rotation of a Kerr black hole by the Blandford-Znajek mechanism. Under this assumption, the first few fractions of a parsec down the jet should be Poynting flux dominated rather than particle dominated. Using variability time arguments, we can estimate the distance of the emission region from the acceleration engine, i.e. SMBH. If the jets are magnetically launched, they must transform to particle dominated by the regions where most of the optical and radio emission originates. It is still unclear how the jets are accelerated and at what point they transform from

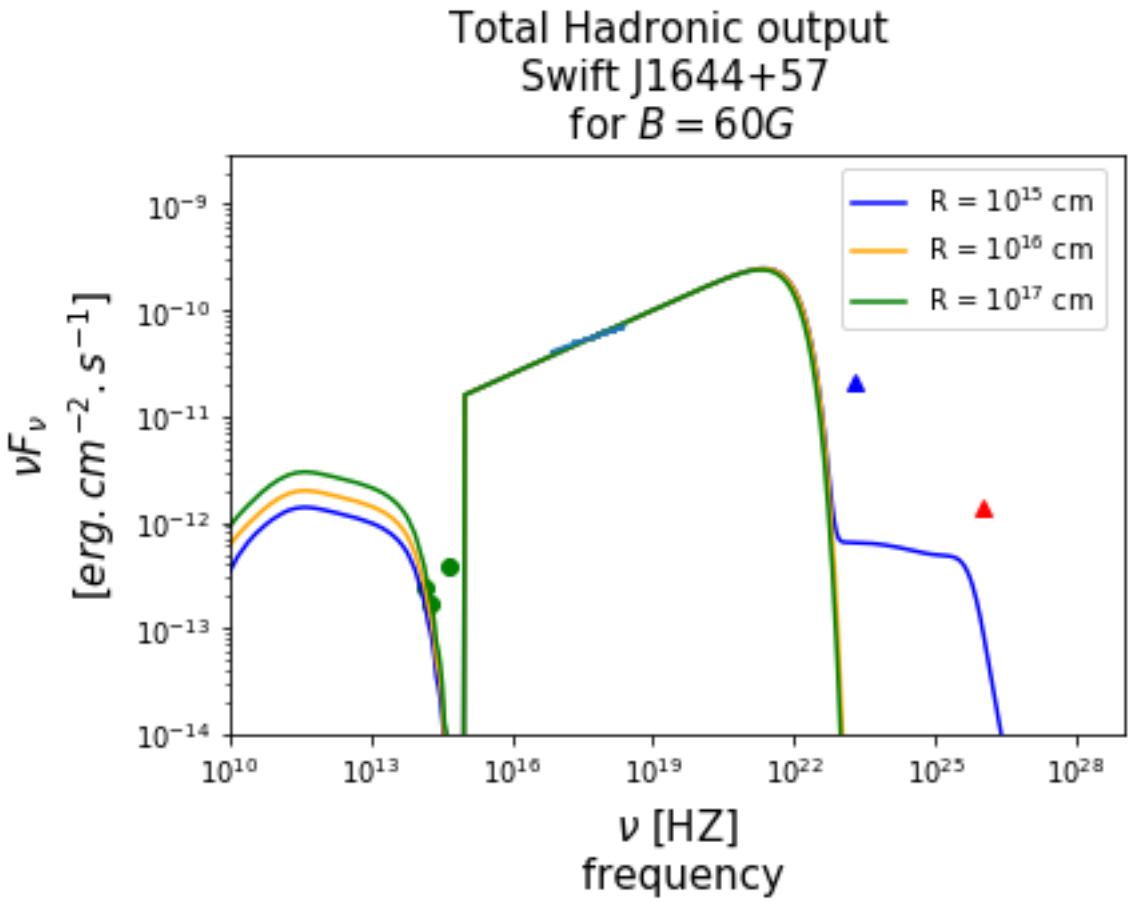

FIGURE 4.6: SED fits with $R_{blob} = 10^{15}$ to 10^{16} and 10^{17} cm with $B = 60G$.

magnetically dominated to particle dominated.

As $\epsilon_{B,p}$ increases , L_p will dominates over L_B and the jet power increases because

$$L \sim 2\pi R^2 \beta_\Gamma c \Gamma^2 (u_B + u_e + u_p) \tag{4.1}$$

where u_B, u_e, u_p are co-moving stationary energy densities of the magnetic field, electron and protons, respectively.

The value of the jet power is not constrained from first principles but may be comparable to the Eddington luminosity L_{edd} as an order of reference. TDEs are in the supper-Eddington regime so we require that acceptable solutions should have $L < L_{edd}$.

In Figure (4.8), we notice that as the magnetic field increases, the magnetization factor becomes larger. We previously mentioned that larger magnetic fields lead to a decrease in the amplitude of the electromagnetic cascade. If B is large and R is small while keeping the flux level constant, the magnetization factor decreases. As ϵ increases the proton-photon interaction becomes more frequent, leading to a more significant electromagnetic bump (see Figure (4.4) and Figure (4.6)). The fit in Figure (4.8) shows that the parameters most likely to produce the cascade components have relatively lower magnetization factors. This suggests that such parameters would

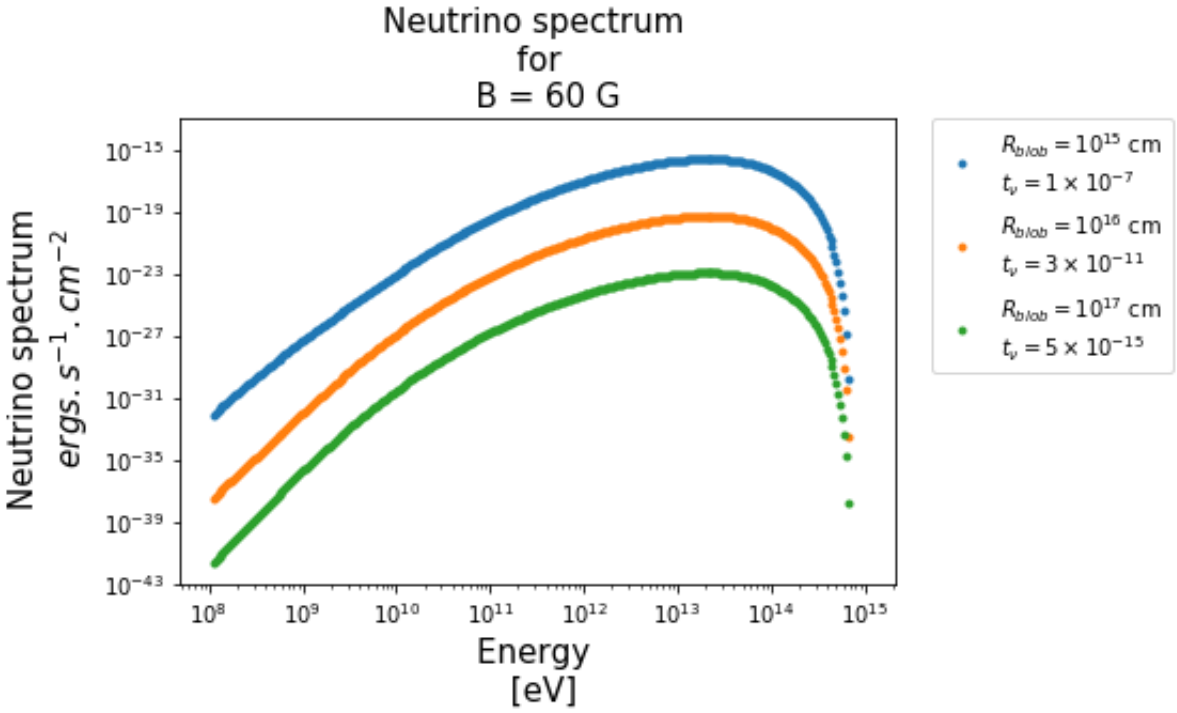

FIGURE 4.7: Neutrino spectra from varying blob radii corresponding to Figure (4.6)

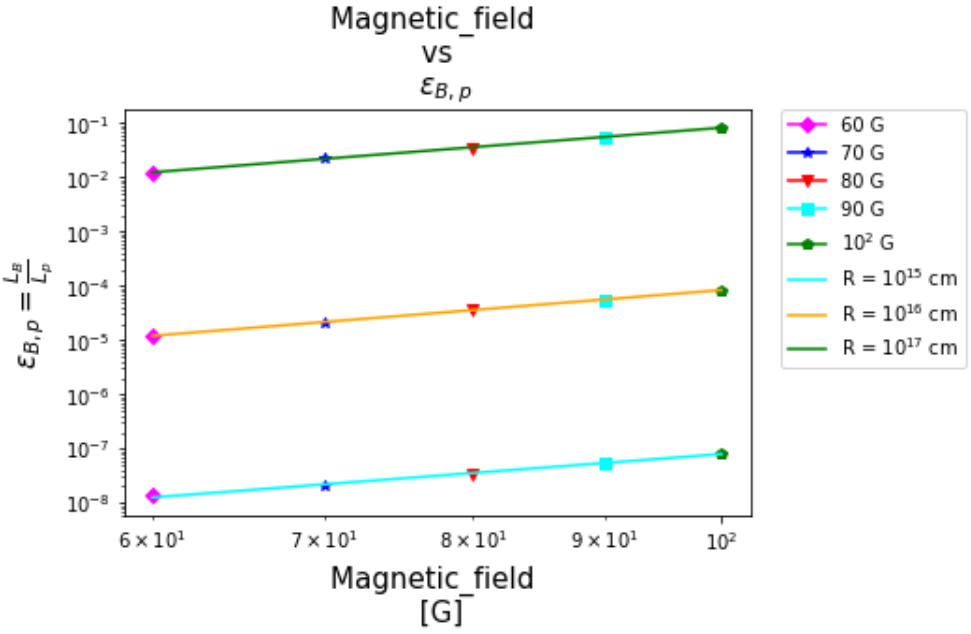

FIGURE 4.8: The log $\epsilon_{B,p}$-log B space: The relationship between the magnetization factor and the magnetic field. As the magnetic field increases $\epsilon_{B,p}$ increases. As you move along (from left to right) the diagonal lines (constant blob radius) one is less likely to produce fits which show significant cascading components.The magnetization factors in the parameter study is $L_p > L_B$this implies that the dissipation might be due to internal shocks (Sikora et al. 2005). This shocks are responsible for particle acceleration.

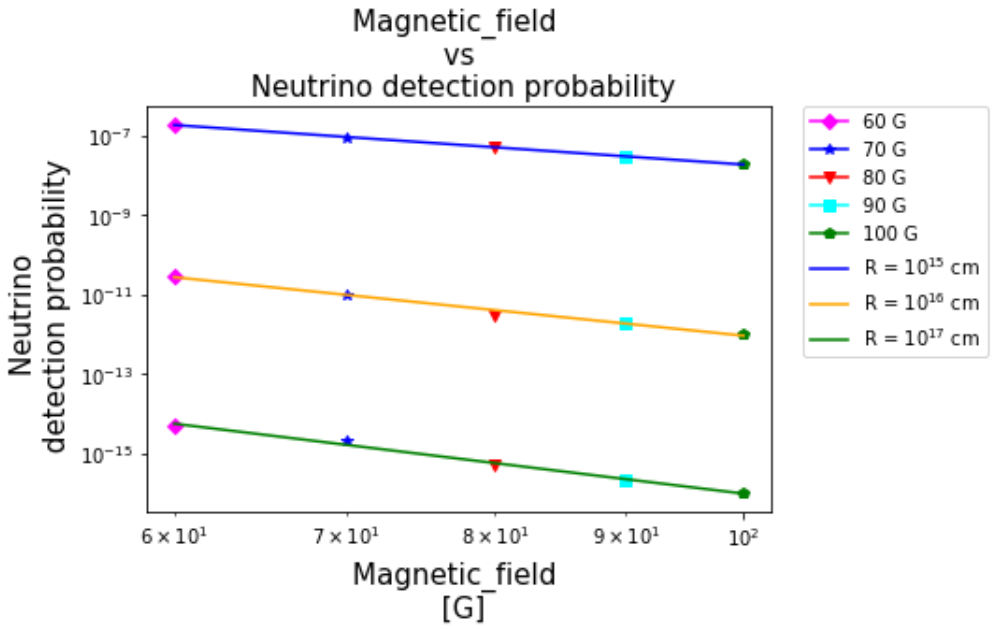

FIGURE 4.9: The comparison plot shows the log-log anti-correlation between the magnetic field and neutrino detection rates. An increase in blob radius results in a vertical shift of the line representing the decline in the neutrino detection rate.

lead to a TDE jet which is proton dominated. We also notice that larger blob radii have had relatively larger magnetization parameters.

The fits in Figure (4.9) shows an anti-correlation between the magnetic field and neutrino detection rate for the different blob radii. This also shows a decrease in the neutrino detection rate with an increase in blob radius, because as the blob radius increases the target photon increases, thus less proton-photon interactions occur. Large values of R_{blob} decrease the optical depth for photopion interactions and neutrino productions.

Chapter 5

Conclusion

In this parameter study, we investigated the relationship between the neutrino production and the characteristic parameters of the TDE, such as the magnetic field strength and the emission region (blob radius). We studied Swift J1644+57, which is one of three jetted TDEs to date. This TDE is X-ray bright and produced a super-Eddington luminosity jet. This source is suitable because of the dense target photon fields present in the jet, which will enable proton-photon interactions. The prediction of neutrino fluxes in astrophysical source models depends on the photohadronic neutrino production. Astrophysical neutrinos are normally assumed to originate from pion decay process.

We used a hadronic jet radiation transfer code to perform this study and saw that the SED produced using the baseline parameters has two well-defined peaks, both from synchrotron radiation of electrons and protons at the optical-X-ray and the $\gamma-$ray energy range, respectively. Whereas the X-rays are from proton synchrotron. A third "tail-like" feature appears at the VHE range as a result of the electromagnetic cascade induced by photohadronic interactions.

Numerous SED fits were produced to investigate the impact varying the magnetic field strength and blob radius would have on the neutrino production. An anti-correlated relationship was noticed between neutrino production and the aforementioned parameters. The anti-correlation between the magnetic field strength and the neutrino probability detection is due to lower energy protons being required to produce the same proton synchrotron photon energies. However, the anti-correlation between the blob radius and the neutrino probability detection is due to a decrease in the target photon field as the blob radius increases.

The neutrino detection rate determines the detection rate of the produced neutrinos which would be detected by the IceCube Observatory. We calculated very low neutrino detection probabilities, with all the neutrino spectra seemingly peaked at $\sim 10TeV$. In the case of the baseline parameters, we calculated a detection probability of 1×10^{-7}. In the parameter study we notice that varying the magnetic field strength gives us a maximum detection probability of 1×10^{-7} for $B = 60$ G and a minimum of 2×10^{-8} when $B = 100$ G, with the blob radius being kept at $R_{blob} = 10^{15}$ cm. Varying the blob radius resulted in a maximum detection of 1×10^{-7} and a minimum of 5×10^{-15} when $R_{blob} = 10^{15}$ and $R_{blob} = 10^{17}$ cm, respectively. These detection probabilities are relatively low, but it is important to note that in this study, we ONLY focused on the peak flaring time of the source whereas neutrinos may also be produced during the afterglow phase.

The code calculated a magnetization parameter for the different parameter values. We noticed an anti-correlated relation between the magnetization factor and the blob radius, implying that the jet would likely be proton dominant. The proton luminosity is also larger than the electron luminosity, suggesting that the magnetic field particle conversion occurs very close to the SMBH.

Our results suggest that X-ray bright jetted TDEs are weak neutrino producing sources, but they could only be responsible for a sub-fraction of the total observed IceCube neutrinos solely because they are extremely rare transient sources and because individual events have a very low neutrino detection rate. In the future, a study to investigate the expected neutrino production between choked and jetted TDEs could prove to be interesting. TDEs are still a poorly understood transient subclass. Therefore there remains a large uncertainty about the rates of TDEs and also the physics and physical parameters involved. Facilities such as the Zwicky Transient Facility (ZTF) and future surveys such as the Large Synoptic Survey Telescope (LSST) should aid the search for transient neutrino analyses. A better understanding of these sources could lead to better source-driven neutrino analysis.

For future work it would be interesting to consider a time-dependent hadronic model approach seeing as the the particle injection luminosity of TDEs varies throughout the lifetime of the event. Additionally, looking at intermediate particle processes such as pion and muon productions would give the model a more holistic view of the electromagnetic cascade than the current framework. Looking at a class based search of jetted and non-jetted TDEs will also allow us to be able to investigate the roles of $p\gamma-$ and $pp-$interactions in possible neutrino producing sites.

Bibliography

Aartsen, M., K. Abraham, M. Ackermann, J. Adams, J. Aguilar, M. Ahlers, M. Ahrens, D. Altmann, T. Anderson, I. Ansseau, et al. 2015. "The IceCube Neutrino Observatory-Contributions to ICRC 2015 Part II: Atmospheric and Astrophysical Diffuse Neutrino Searches of All Flavors." *arXiv preprint arXiv:1510.05223.*

Collaboration, I., et al. 2018. "Neutrino emission from the direction of the blazar TXS 0506+ 056 prior to the IceCube-170922A alert." *Science* 361 (6398): 147–151.

Dumm, J. P. 2011. "Searches for Point-like Sources of Neutrinos with the 40-String IceCube Detector."

Bednarek, W., G. F. Burgio, and T. Montaruli. 2005. "Galactic discrete sources of high energy neutrinos." *New Astronomy Reviews* 49 (1): 1–21.

Waxman, E. 2007. "Neutrino astrophysics: A new tool for exploring the universe." *Science* 315 (5808): 63–65.

Becker, J. K. 2008. "Status of neutrino astronomy." In *Journal of Physics: Conference Series,* 136:022055. 2. IOP Publishing.

Mannheim, K. 1993. "The proton blazar." *arXiv preprint astro-ph/9302006.*

Waxman, E., and J. Bahcall. 1997. "High energy neutrinos from cosmological gamma-ray burst fireballs." *Physical Review Letters* 78 (12): 2292.

Tamborra, I., and S. Ando. 2015. "Diffuse emission of high-energy neutrinos from gamma-ray burst fireballs." *Journal of Cosmology and Astroparticle Physics* 2015 (09): 036.

Davis Jr, R., D. S. Harmer, and K. C. Hoffman. 1968. "Search for neutrinos from the sun." *Physical Review Letters* 20 (21): 1205.

Burrows, A., and J. M. Lattimer. 1987. "Neutrinos from SN 1987A." *The Astrophysical Journal* 318:L63–L68.

Wang, X.-Y., R.-Y. Liu, Z.-G. Dai, and K. Cheng. 2011. "Probing the tidal disruption flares of massive black holes with high-energy neutrinos." *Physical Review D* 84 (8): 081301.

Wang, X.-Y., and R.-Y. Liu. 2016. "Tidal disruption jets of supermassive black holes as hidden sources of cosmic rays: explaining the IceCube TeV-PeV neutrinos." *Physical Review D* 93 (8): 083005.

Dai, L., J. C. McKinney, and M. C. Miller. 2015. "Soft x-ray temperature tidal disruption events from stars on deep plunging orbits." *The Astrophysical Journal Letters* 812 (2): L39.

Senno, N., K. Murase, and P. Mészáros. 2017. "High-energy neutrino flares from X-ray bright and dark tidal disruption events." *The Astrophysical Journal* 838 (1): 3.

Lunardini, C., and W. Winter. 2017. "High energy neutrinos from the tidal disruption of stars." *Physical Review D* 95 (12): 123001.

Guépin, C., K. Kotera, E. Barausse, K. Fang, and K. Murase. 2018. "Ultra-high-energy cosmic rays and neutrinos from tidal disruptions by massive black holes." *Astronomy & Astrophysics* 616:A179.

Biehl, D., A. Fedynitch, A. Palladino, T. J. Weiler, and W. Winter. 2017. "Astrophysical neutrino production diagnostics with the Glashow resonance." *Journal of Cosmology and Astroparticle Physics* 2017 (01): 033.

Stein, R., S. van Velzen, M. Kowalski, A. Franckowiak, S. Gezari, J. C. Miller-Jones, S. Frederick, I. Sfaradi, M. F. Bietenholz, A. Horesh, et al. 2020. "A high-energy neutrino coincident with a tidal disruption event." *arXiv preprint arXiv:2005.05340.*

Hills, J. 1975. "Possible power source of Seyfert galaxies and QSOs." *Nature* 254 (5498): 295.

Rees, M. J. 1988. "Tidal disruption of stars by black holes of 106–108 solar masses in nearby galaxies." *Nature* 333 (6173): 523.

Lacy, J. H., C. H. Townes, and D. J. Hollenbach. 1982. "The nature of the central parsec of the Galaxy." *The Astrophysical Journal* 262:120–134.

Phinney, E. 1989. "Manifestations of a massive black hole in the galactic center." In *The Center of the Galaxy*, 543–553. Springer.

Farrar, G. R., and T. Piran. 2014. "Tidal disruption jets as the source of Ultra-High Energy Cosmic Rays." *arXiv preprint arXiv:1411.0704.*

Blandford, R., M. Rees, and A. Wolfe. 1978. "Pittsburgh conference on BL Lac objects." *AM Wolfe, Ed* 328.

Hardee, P. 1979. "On the configuration and propagation of jets in extragalactic radio sources." *The Astrophysical Journal* 234:47–55.

Velzen, S. van, N. C. Stone, B. D. Metzger, S. Gezari, T. M. Brown, and A. S. Fruchter. 2019. "Late-time UV Observations of Tidal Disruption Flares Reveal Unobscured, Compact Accretion Disks." *ApJ* 878 (2): 82.

Böttcher, M., A. Reimer, K. Sweeney, and A. Prakash. 2013. "Leptonic and hadronic modeling of Fermi-detected blazars." *The Astrophysical Journal* 768 (1): 54.

Soares-Santos, M., D. Holz, J. Annis, R. Chornock, K. Herner, E. Berger, D. Brout, H.-Y. Chen, R. Kessler, M. Sako, et al. 2017. "The electromagnetic counterpart of the binary neutron star merger LIGO/Virgo GW170817. I. Discovery of the optical counterpart using the dark energy camera." *The Astrophysical Journal Letters* 848 (2): L16.

Collaboration, I., et al. 2013. "Evidence for high-energy extraterrestrial neutrinos at the IceCube detector." *Science* 342 (6161): 1242856.

Shawhan, P. S. 2018. "Multi-Messenger Astrophysics."

Fowler, W. A. 1956. "Experimental and Observational Evidence for Origin of the Elements in Stars." *Publications of the Astronomical Society of the Pacific* 68:505.

Formaggio, J. A., and G. Zeller. 2012. "From eV to EeV: Neutrino cross sections across energy scales." *Reviews of Modern Physics* 84 (3): 1307.

Mannheim, K., and P. Biermann. 1992. "Gamma-ray flaring of 3C 279-A proton-initiated cascade in the jet?" *Astronomy and Astrophysics* 253:L21–L24.

Mucke, A., J. Rachen, T. Stanev, R. Protheroe, and R. Engel. 1999. "Photohadronic processes in astrophysical environments." *Publications of the Astronomical Society of Australia* 16 (2): 160–166.

Pakvasa, S. 2008. "Neutrino flavor goniometry by high energy astrophysical beams." *Modern Physics Letters A* 23 (17n20): 1313–1324.

Stecker, F. 1973. "Ultrahigh energy photons, electrons, and neutrinos, the microwave background, and the universal cosmic-ray hypothesis." *Astrophysics and Space Science* 20 (1): 47–57.

Bouwhuis, M. C. 2005. *Detection of neutrinos from gamma-ray bursts.* Technical report.

Abreu, P., M. Aglietta, M. Ahlers, E. Ahn, I. Albuquerque, D. Allard, I. Allekotte, J. Allen, P. Allison, A. Almela, et al. 2011. "Search for ultrahigh energy neutrinos in highly inclined events at the Pierre Auger Observatory." *Physical Review D* 84 (12): 122005.

Madsen, J. 2019. "Ultra-High Energy Neutrinos." *arXiv preprint arXiv:1901.02528.*

Aartsen, M., M. Ackermann, J. Adams, J. Aguilar, M. Ahlers, M. Ahrens, D. Altmann, K. Andeen, T. Anderson, I. Ansseau, et al. 2017. "The IceCube realtime alert system." *Astroparticle Physics* 92:30–41.

Stone, N. C. 2014. *The Tidal Disruption of Stars by Supermassive Black Holes: An Analytic Approach.* Springer.

Wheeler, J. 1971. "Mechanism for Jets." In *Study Week on Nuclei of Galaxies,* 539.

Evans, C. R., and C. S. Kochanek. 1989. "The tidal disruption of a star by a massive black hole." *The Astrophysical Journal* 346:L13–L16.

Müller, A. 2007. "Experimental evidence of black holes." *arXiv preprint astro-ph/0701228.*

Stone, N., and A. Loeb. 2012. "Tidal disruption flares of stars from moderately recoiled black holes." *Monthly Notices of the Royal Astronomical Society* 422 (3): 1933–1947.

Shen, R.-F., and C. D. Matzner. 2014. "Evolution of accretion disks in tidal disruption events." *The Astrophysical Journal* 784 (2): 87.

Kesden, M. 2012. "Tidal-disruption rate of stars by spinning supermassive black holes." *Physical Review D* 85 (2): 024037.

Leloudas, G., M. Fraser, N. Stone, S. van Velzen, P. Jonker, I. Arcavi, C. Fremling, J. Maund, S. Smartt, T. Krıhler, et al. 2016. "The superluminous transient ASASSN-15lh as a tidal disruption event from a Kerr black hole." *Nature Astronomy* 1 (1): 1–8.

Beloborodov, A., A. Illarionov, P. Ivanov, and A. Polnarev. 1992. "Angular momentum of a supermassive black hole in a dense star cluster." *Monthly Notices of the Royal Astronomical Society* 259 (2): 209–217.

Dai, L., and K. Fang. 2017. "Can tidal disruption events produce the IceCube neutrinos?" *Monthly Notices of the Royal Astronomical Society* 469 (2): 1354–1359.

Pasham, D. R., S. B. Cenko, A. J. Levan, G. C. Bower, A. Horesh, G. C. Brown, S. Dolan, K. Wiersema, A. V. Filippenko, A. S. Fruchter, et al. 2015. "A multiwavelength study of the relativistic tidal disruption candidate Swift J2058. 4+ 0516 at late times." *The Astrophysical Journal* 805 (1): 68.

Bower, G. C., B. D. Metzger, S. B. Cenko, J. M. Silverman, and J. S. Bloom. 2013. "Late-time radio emission from x-ray-selected tidal disruption events." *The Astrophysical Journal* 763 (2): 84.

Ageron, M., J. Aguilar, I. Al Samarai, A. Albert, F. Ameli, M. André, M. Anghinolfi, G. Anton, S. Anvar, M. Ardid, et al. 2011. "ANTARES: the first undersea neutrino telescope." *Nuclear Instruments and Methods in Physics Research Section A: Accelerators, Spectrometers, Detectors and Associated Equipment* 656 (1): 11–38.

Gezari, S., R. Chornock, A. Lawrence, A. Rest, D. Jones, E. Berger, P. Challis, and G. Narayan. 2015. "PS1-10jh continues to follow the fallback accretion rate of a tidally disrupted star." *The Astrophysical Journal Letters* 815 (1): L5.

Holoien, T.-S., J. Prieto, D. Bersier, C. Kochanek, K. Stanek, B. Shappee, D. Grupe, U. Basu, J. Beacom, J. Brimacombe, et al. 2014. "ASASSN-14ae: a tidal disruption event at 200 Mpc." *Monthly Notices of the Royal Astronomical Society* 445 (3): 3263–3277.

Gezari, S., D. Martin, B. Milliard, S. Basa, J. Halpern, K. Forster, P. Friedman, P. Morrissey, S. Neff, D. Schiminovich, et al. 2006. "Ultraviolet detection of the tidal disruption of a star by a supermassive black hole." *The Astrophysical Journal Letters* 653 (1): L25.

Peng, F.-K., Q.-W. Tang, and X.-Y. Wang. 2016. "Search for High-energy Gamma-ray Emission from Tidal Disruption Events with the Fermi Large Area Telescope." *The Astrophysical Journal* 825 (1): 47.

Graham, M. J., S. Kulkarni, E. C. Bellm, S. M. Adams, C. Barbarino, N. Blagorodnova, D. Bodewits, B. Bolin, P. R. Brady, S. B. Cenko, et al. 2019. "The Zwicky transient facility: science objectives." *Publications of the Astronomical Society of the Pacific* 131 (1001): 078001.

Merloni, A., P. Predehl, W. Becker, H. Böhringer, T. Boller, H. Brunner, M. Brusa, K. Dennerl, M. Freyberg, P. Friedrich, et al. 2012. "eROSITA science book: mapping the structure of the energetic universe." *arXiv preprint arXiv:1209.3114.*

Ivezic, Z., J. Tyson, T. Axelrod, D. Burke, C. Claver, K. Cook, S. Kahn, R. Lupton, D. Monet, P. Pinto, et al. 2009. "LSST: from science drivers to reference design and anticipated data products." In *Bulletin of the American Astronomical Society*, 41:366.

Burrows, D. N., J. A. Kennea, G. Ghisellini, V. Mangano, B. Zhang, K. Page, M. Eracleous, P. Romano, T. Sakamoto, A. D. Falcone, et al. 2011. "Relativistic jet activity from the tidal disruption of a star by a massive black hole." *Nature* 476 (7361): 421–424.

Bloom, J. S., D. Giannios, B. D. Metzger, S. B. Cenko, D. A. Perley, N. R. Butler, N. R. Tanvir, A. J. Levan, P. T. O'Brien, L. E. Strubbe, et al. 2011. "A possible relativistic jetted outburst from a massive black hole fed by a tidally disrupted star." *Science* 333 (6039): 203–206.

Zauderer, B. A., E. Berger, A. M. Soderberg, A. Loeb, R. Narayan, D. Frail, G. R. Petitpas, A. Brunthaler, R. Chornock, J. Carpenter, et al. 2011. "Birth of a relativistic outflow in the unusual γ-ray transient Swift J164449. 3+ 573451." *Nature* 476 (7361): 425.

Levan, A. J., N. R. Tanvir, S. B. Cenko, D. A. Perley, K. Wiersema, J. S. Bloom, A. S. Fruchter, A. de Ugarte Postigo, P. O'Brien, N. Butler, et al. 2011. "An extremely luminous panchromatic outburst from the nucleus of a distant galaxy." *Science* 333 (6039): 199–202.

De Colle, F., and W. Lu. 2019. "Jets from Tidal Disruption Events." *arXiv preprint arXiv:1911.01442.*

Komossa, S., and D. Merritt. 2008. "Tidal disruption flares from recoiling supermassive black holes." *The Astrophysical Journal Letters* 683 (1): L21.

Zauderer, B., E. Berger, R. Margutti, G. Pooley, R. Sari, A. M. Soderberg, A. Brunthaler, and M. Bietenholz. 2013. "Radio monitoring of the tidal disruption event Swift J164449. 3+ 573451. II. The relativistic jet shuts off and a transition to forward shock X-ray/radio emission." *The Astrophysical Journal* 767 (2): 152.

Cenko, S. B., H. A. Krimm, A. Horesh, A. Rau, D. A. Frail, J. A. Kennea, A. J. Levan, S. T. Holland, N. R. Butler, R. M. Quimby, et al. 2012. "Swift J2058. 4+ 0516: Discovery of a possible second relativistic tidal disruption flare?" *The Astrophysical Journal* 753 (1): 77.

Bade, N., S. Komossa, and M. Dahlem. 1996. "Detection of an extremely soft X-ray outburst in the HII-like nucleus of NGC 5905." *Astronomy and Astrophysics* 309:L35–L38.

Grupe, D., H.-C. Thomas, and K. Leighly. 1999. "RX J1624. 9+ 7554: a new X-ray transient AGN." *arXiv preprint astro-ph/9909101.*

Komossa, S., and J. Greiner. 1999. "Discovery of a giant and luminous X-ray outburst from the optically inactive galaxy pair RXJ1242. 6-1119." *arXiv preprint astro-ph/9908216.*

Reis, R. C., J. Miller, M. Reynolds, K. Gültekin, D. Maitra, A. King, and T. Strohmayer. 2012. "A 200-second quasi-periodicity after the tidal disruption of a star by a dormant black hole." *Science* 337 (6097): 949–951.

Komossa, S. 2012. "Tidal disruption of stars by supermassive black holes: The X-ray view." In *EPJ Web of Conferences*, 39:02001. EDP Sciences.

Wiersema, K., A. van der Horst, A. Levan, N. Tanvir, R. Karjalainen, A. Kamble, C. Kouveliotou, B. Metzger, D. Russell, I. Skillen, et al. 2012. "Polarimetry of the transient relativistic jet of GRB 110328/Swift J164449. 3+ 573451." *Monthly Notices of the Royal Astronomical Society* 421 (3): 1942–1948.

Stern, D., P. Van Dokkum, P. Nugent, D. Sand, R. Ellis, M. Sullivan, J. Bloom, D. Frail, J.-P. Kneib, L. Koopmans, et al. 2004. "Discovery of a transient U-band dropout in a Lyman break survey: A tidally disrupted star at z= 3.3?" *The Astrophysical Journal* 612 (2): 690.

Tchekhovskoy, A., B. D. Metzger, D. Giannios, and L. Z. Kelley. 2013. "Swift J1644+ 57 gone MAD: the case for dynamically important magnetic flux threading the black hole in a jetted tidal disruption event." *Monthly Notices of the Royal Astronomical Society* 437 (3): 2744–2760.

Eftekhari, T., E. Berger, B. Zauderer, R. Margutti, and K. Alexander. 2018. "Radio Monitoring of the Tidal Disruption Event Swift J164449. 3+ 573451. III. Late-time Jet Energetics and a Deviation from Equipartition." *The Astrophysical Journal* 854 (2): 86.

Krolik, J. H., and T. Piran. 2012. "Jets from tidal disruptions of stars by black holes." *The Astrophysical Journal* 749 (1): 92.

Shao, L., F.-W. Zhang, Y.-Z. Fan, and D.-M. Wei. 2011. "Sw 1644+ 57/GRB 110328A: the physical origin and the composition of the relativistic outflow." *The Astrophysical Journal Letters* 734 (2): L33.

Cannizzo, J. K., E. Troja, and G. Lodato. 2011. "GRB 110328A/Swift J164449. 3+ 573451: the tidal obliteration of a deeply plunging star?" *The Astrophysical Journal* 742 (1): 32.

Piran, T., A. Sądowski, and A. Tchekhovskoy. 2015. "Jet and disc luminosities in tidal disruption events." *Monthly Notices of the Royal Astronomical Society* 453 (1): 157–165.

Piran, T., G. Svirski, J. Krolik, R. M. Cheng, and H. Shiokawa. 2015. "DISK FORMATION VERSUS DISK ACCRETION—WHAT POWERS TIDAL DISRUPTION EVENTS?" *The Astrophysical Journal* 806 (2): 164.

Mandel, I., and Y. Levin. 2015. "Double tidal disruptions in galactic nuclei." *The Astrophysical Journal Letters* 805 (1): L4.

Kara, E., J. M. Miller, C. Reynolds, and L. Dai. 2016. "Relativistic reverberation in the accretion flow of a tidal disruption event." *Nature* 535 (7612): 388.

Stone, N. C., and B. D. Metzger. 2015. "Rates of stellar tidal disruption as probes of the supermassive black hole mass function." *Monthly Notices of the Royal Astronomical Society* 455 (1): 859–883.

Blandford, R. D., and R. L. Znajek. 1977. "Electromagnetic extraction of energy from Kerr black holes." *Monthly Notices of the Royal Astronomical Society* 179 (3): 433–456.

Penrose, R. 1969. "Riv Nuovo Cimento 1, 252." *General Relativity, an Einstein Centenary Volume.*

Jefremov, P. I., O. Y. Tsupko, and G. S. Bisnovatyi-Kogan. 2015. "Innermost stable circular orbits of spinning test particles in Schwarzschild and Kerr space-times." *Physical Review D* 91 (12): 124030.

Paczynsky, B., and P. J. Wiita. 1980. "Thick accretion disks and supercritical luminosities." *Astronomy and Astrophysics* 88:23–31.

Blandford, R. D., and M. C. Begelman. 1999. "On the fate of gas accreting at a low rate on to a black hole." *Monthly Notices of the Royal Astronomical Society* 303 (1): L1–L5.

Kelley, L. Z., A. Tchekhovskoy, and R. Narayan. 2014. "Tidal disruption and magnetic flux capture: Powering a jet from a quiescent black hole." *Monthly Notices of the Royal Astronomical Society* 445 (4): 3919–3938.

Ivanov, P. B., A. Polnarev, and P. Saha. 2005. "The tidal disruption rate in dense galactic cusps containing a supermassive binary black hole." *Monthly Notices of the Royal Astronomical Society* 358 (4): 1361–1378.

Strubbe, L. E., and E. Quataert. 2011. "Spectroscopic signatures of the tidal disruption of stars by massive black holes." *Monthly Notices of the Royal Astronomical Society* 415 (1): 168–180.

Lei, W.-H., B. Zhang, and H. Gao. 2012. "Frame dragging, disk warping, jet precessing, and dipped X-ray light curve of Sw J1644+ 57." *The Astrophysical Journal* 762 (2): 98.

Loeb, A., and A. Ulmer. 1997. "Optical appearance of the debris of a star disrupted by a massive black hole." *The Astrophysical Journal* 489 (2): 573.

Rybicki, G. B., and A. P. Lightman. 2008. *Radiative processes in astrophysics.* John Wiley & Sons.

Böttcher, M., D. E. Harris, and H. Krawczynski. 2012. *Relativistic Jets from Active Galactic Nuclei.* Vol. 1. Wiley Online Library.

Gaisser, T. K., R. Engel, and E. Resconi. 2016. *Cosmic rays and particle physics.* Cambridge University Press.

Bell, A. 1978. "The acceleration of cosmic rays in shock fronts–I." *Monthly Notices of the Royal Astronomical Society* 182 (2): 147–156.

Blandford, R. D., and J. P. Ostriker. 1978. "Particle acceleration by astrophysical shocks." *The Astrophysical Journal* 221:L29–L32.

Mücke, A., R. Engel, J. Rachen, R. Protheroe, and T. Stanev. 2000. "Monte Carlo simulations of photohadronic processes in astrophysics." *Computer Physics Communications* 124 (2-3): 290–314.

Kelner, S., and F. Aharonian. (2008). "Energy spectra of gamma rays, electrons, and neutrinos produced at interactions of relativistic protons with low energy radiation." *Physical Review D* 78 (3): 034013.

Mücke, A., R. Protheroe, R. Engel, J. Rachen, and T. Stanev. 2003. "BL Lac objects in the synchrotron proton blazar model." *Astroparticle Physics* 18 (6): 593–613.

Hayasaki, K., N. Stone, and A. Loeb. 2016. "Circularization of tidally disrupted stars around spinning supermassive black holes." *Monthly Notices of the Royal Astronomical Society* 461 (4): 3760–3780.

Levan, A., N. Tanvir, G. Brown, B. Metzger, K. Page, S. Cenko, P. O'Brien, J. Lyman, K. Wiersema, E. Stanway, et al. 2016. "Late Time Multi-wavelength Observations of Swift J1644+ 5734: A Luminous Optical/IR Bump and Quiescent X-Ray Emission." *The Astrophysical Journal* 819 (1): 51.

Grupen, C., G. Cowan, S. Eidelman, and T. Stroh. 2005. *Astroparticle physics.* Vol. 50. Springer.

Ghisellini, G. 2013. *Radiative processes in high energy astrophysics.* Vol. 873. Springer.

Oikonomou, F., K. Murase, P. Padovani, E. Resconi, and P. Mészáros. 2019. "High-energy neutrino flux from individual blazar flares." *Monthly Notices of the Royal Astronomical Society* 489 (3): 4347–4366.

Crumley, P., D. Caprioli, S. Markoff, and A. Spitkovsky. 2019. "Kinetic simulations of mildly relativistic shocks–I. Particle acceleration in high Mach number shocks." *Monthly Notices of the Royal Astronomical Society* 485 (4): 5105–5119.

Barkov, M. V., F. A. Aharonian, S. V. Bogovalov, S. R. Kelner, and D. Khangulyan. 2012. "Rapid TeV variability in blazars as a result of jet-star interaction." *The Astrophysical Journal* 749 (2): 119.

Aharonian, F. 2000. "TeV gamma rays from BL Lac objects due to synchrotron radiation of extremely high energy protons." *New Astronomy* 5 (7): 377–395.

Sikora, M., M. C. Begelman, G. M. Madejski, and J.-P. Lasota. 2005. "Are quasar jets dominated by Poynting flux?" *The Astrophysical Journal* 625 (1): 72.

Sakurai, T. 1987. "Magnetically collimated winds from accretion disks." *Publications of the Astronomical Society of Japan* 39:821–835.

Beskin, V., I. Kuznetsova, and R. Rafikov. 1998. "On the MHD effects on the force-free monopole outflow." *Monthly Notices of the Royal Astronomical Society* 299 (2): 341–348.

Hughes, P., H. Aller, and M. Aller. 1989. "Synchrotron emission from shocked relativistic jets. I-The theory of radio-wavelength variability and its relation to superluminal motion." *The Astrophysical Journal* 341:54–79.